JOURNAL OF GEOPHYSICAL RESEARCH, VOL. 108, NO. D4, 4142, doi:10.1029/2001JD001494, 2003

Transport and mixing between airmasses in cold frontal regions during Dynamics and Chemistry of Frontal Zones (DCFZ)

J. G. Esler,[1,2] P. H. Haynes,[1] K. S. Law,[3] H. Barjat,[4] K. Dewey,[4] J. Kent,[4] S. Schmitgen,[5,6]
and N. Brough[7]

Received 13 November 2001; revised 30 April 2002; accepted 3 May 2002; published 27 February 2003.

[1] The passage of two cold front systems over the United Kingdom are compared and contrasted, using the results of a detailed aircraft and ground-based study. The measurements are interpreted by means of three-dimensional, reverse-domain-filling trajectories using both global models and limited-area mesoscale models. This method provides a three-dimensional picture of the interleaving air-masses in the frontal zone as defined by their Lagrangian histories. The two systems studied differ in that the first is associated with an intense surface low in January and the second is associated with a relatively weak surface low in April. In the intense surface low case the trajectory study suggests that a dry intrusion with stratospheric characteristics penetrated deep into the troposphere along the upper level front. Measurements indeed revealed an unsaturated layer with anomalously high ozone. This layer was intersected at four levels in the troposphere (at 8.5, 7.1, 5.2 and 3.7 km), and the lower the intersection, the lower the measured anomalous ozone and the higher the water vapor content. It is argued that this is best explained by the dry-intrusion layer becoming mixed with background air by three-dimensional turbulence, also encountered by the aircraft, along the upper level front. Evidence for this mixing is apparent on tracer-tracer scatterplots. In the weak surface low case, by contrast, the dry intrusion has a more complex structure, with up to three separate layers of enhanced ozone and low humidity. Strong evidence for mixing was apparent only in the lowest layer. The weaker system may therefore be much more efficient at transporting upper tropospheric/stratospheric ozone to the lower troposphere. The transport of boundary layer air to the upper troposphere in the warm conveyor belt (WCB), however, was found to be around 8 times stronger in the intense system. Sonde measurements suggested that the WCB was ventilated by convection from the surface front in some regions to about 5–6 km, while it was stably stratified in other regions, suggesting layerwise long-range transport. *INDEX TERMS:* 0365 Atmospheric Composition and Structure: Troposphere—composition and chemistry; 0368 Atmospheric Composition and Structure: Troposphere—constituent transport and chemistry; 3314 Meteorology and Atmospheric Dynamics: Convective processes; *KEYWORDS:* frontal zones, chemistry and mixing

Citation: Esler, J. G., P. H. Haynes, K. S. Law, H. Barjat, K. Dewey, J. Kent, S. Schmitgen, and N. Brough, Transport and mixing between airmasses in cold frontal regions during Dynamics and Chemistry of Frontal Zones (DCFZ), *J. Geophys. Res.*, *108*(D4), 4142, doi:10.1029/2001JD001494, 2003.

1. Introduction

[2] There has been much recent interest [e.g., *Newell et al.*, 1999, and references therein; *Thouret et al.*, 2000] in the near-ubiquitous, layered structure of observed airmasses in the extratropical troposphere. Frontal zones are, by definition, boundaries between airmasses, and a knowledge of the detailed structure of these regions is necessarily of great importance in understanding the relative roles of transport and chemistry in the budgets of trace gases [*Bethan et al.*, 1998]. Transport in the main ascending branch of an extratropical cyclone, the warm conveyor belt [*Browning*, 1990], has recently been argued to be one of the main mechanisms for transporting boundary layer air into the upper troposphere in midlatitudes [*Stohl*, 2001; *Cooper et al.*, 2001]. Similarly, the dry intrusion [*Cooper et al.*, 1998;

---

[1] Department of Applied Mathematics and Theoretical Physics, Centre for Atmospheric Science, University of Cambridge, Cambridge, U.K.

[2] Now at Department of Mathematics, University College London, London, U.K.

[3] Department of Chemistry, Centre for Atmospheric Science, University of Cambridge, Cambridge, U.K.

[4] Met Research Flight, U.K. Met Office, Farnborough, Hampshire, U.K.

[5] Institut für Chemie und Dynamik der Geosphaere, Forschungszentrum Jülich, Germany.

[6] Now at Laboratoire des Sciences du Climat et de l'Environnement, UMR CEA/CNRS, Gif-sur-Yvette, France.

[7] School of Environmental Sciences, University of East Anglia, Norwich, U.K.

0148-0227/03/2001JD001494

Stohl and Trickl, 1999] transports dry, ozone-rich air downward from tropopause level to the lower troposphere. The cold frontal zone represents the boundary between these two airmasses, so mixing in this region can potentially bring together moist, polluted air and air with a stratospheric signature. *Esler et al.* [2001] have recently shown that mixing between airmasses with such contrasting origins could have implications for the mean concentrations of hydroxyl (OH) radical and can therefore affect the budget of many trace gases.

[3] During the Dynamics and Chemistry of Frontal Zones (DCFZ) project (January 8 through April 10, 1999) 20 frontal zones passing over the United Kingdom were investigated. Most of the fronts encountered were embedded in one of around 25 extratropical cyclones passing eastward over or near the United Kingdom during the campaign. The principal aims of DCFZ included determining the relative positions and origins of the distinct airmasses in each frontal zone, the extent of mixing between the airmasses, and the chemical implications of this mixing. Radar and ozonesonde measurements (from Aberystwyth, −4.10°E, 52.40°N) were made routinely throughout the campaign and for selected cases in situ measurements were made on board aircraft flights (six in total). This paper will concentrate on two such flights (1 and 6). Figure 1 shows flight paths of the Hercules C-130 aircraft and the orientation of the fronts in each case. During both flights the aircraft crossed northeast-southwest oriented cold frontal zones, although the synoptic situation differed. Flight 6 intersected a weak cold front embedded in a relatively weak cyclonic system, typical of many cases encountered during DCFZ. By contrast,flight 1 took place through a stronger front embedded in a strong cyclonic system: only approximately four cyclones of comparable intensity passed over the United Kingdom during the 3-month campaign period.

[4] Much work has focused on the structure of extratropical cyclones from the point of view of forecasting precipitation. *Carlson* [1980] presented a standard model of an extratropical cyclone based on the observation that clear boundaries between airmasses emerge when the isentropic flow relative to the motion of the front is considered. At the cold front, this boundary is between the warm conveyor belt and dry intrusion. Carlson's model and subsequent work have been reviewed in detail by *Browning* [1990]; see in particular his Figure 8.9. Other relevant case studies have focused on the mesoscale structure of the dry intrusion [*Browning and Golding*, 1995] and on surface cold front cyclogenesis [*Browning et al.*, 1997].

[5] There have been several modeling studies concentrating on transport by frontal circulations, based on both idealized baroclinic wave life cycles [*Wang and Shallcross*, 2000; *Stone et al.*, 1999] and on observed events [*Chaumerliac et al.*, 1992; *Gimson*, 1994; *Donnell et al.*, 2001]. The latter study focused on the frontal circulation encountered during flight 1 of DCFZ as one case study. They were interested in the mechanisms for transport from the boundary layer to the free troposphere, and found that advective transport in the WCB by the large-scale winds was the principal mechanism, with convection and turbulent mixing playing lesser but still significant roles. Convection was found to be strongest in the region behind the cold front where boundary layer air was lifted to 3–4 km, much lower than the air transported in the WCB.

[6] These results underline the relevance to chemical transport of recent trajectory-based analysis of Lagrangian transport in extratropical cyclones [*Wernli*, 1997; *Wernli and Davies*, 1997; *Stohl and Trickl*, 1999]. *Wernli* [1997] showed that trajectories typically form several distinct "coherent ensembles" that have similar properties and/or origin. In this paper we aim to develop such methodology, using back trajectories in conjunction with the reverse-domain-filling (RDF) technique [*Sutton et al.*, 1994]. This allows us to present Lagrangian airmass properties on distance-height cross-sections spanning the frontal zone. Examples of relevant quantities include the change of parcel height over several hours or days, direction of parcel origin, and previous potential vorticity values (indicating stratospheric origin). Use of the RDF technique allows easy inspection of the relative dimensions of the airmasses and the "gradients" in Lagrangian properties that exist between them.

[7] The DCFZ mission allows a unique opportunity to compare results from the above techniques with measurements from aircraft flights that have been specifically planned to intersect cold frontal zone airmasses over the United Kingdom. Airmasses identified in the trajectory analysis were crossed repeatedly, at different locations and heights by the aircraft and ozone sondes, allowing inferences to be made about the mixing of air as it moved through the airmass. This contrasts with previous "out and back" flights, such as those reported by *Bethan et al.* [1998], from which it is more difficult to determine the orientation of boundaries between airmasses and their aspect ratio. The aim of this paper is to exploit these measurements to build as detailed a picture as possible of airmass structure and evolution in cold frontal zones. In section 2 the synoptic situation at the time of each of the flights is discussed, while in section 3 the measurements taken during DCFZ and methodology used to interpret them, including the trajectory analysis method, is described. In section 4, the results from flight 1, which took place through the more intense cyclonic system will be described and analyzed. The flight 6 case through the weaker system will be discussed in section 5. Finally, in section 6 we present our conclusions.

2. Synoptic Situation

[8] Figure 2 shows a snapshot of the synoptic situation during the two flights. The top panels show ECMWF sea level pressure (contours) along with surface wet-bulb potential temperature θ_w (shading) calculated from ECMWF wind fields. The lower panels show −1.5 day RDF Ertel's potential vorticity (PV hereafter) on an isentropic surface, along with the geopotential height, in kilometers, of that surface.

[9] For flight 1 the surface θ_w field clearly reveals a surface cold front oriented SW-NE over the United Kingdom. The front is part of an intense cyclonic system with surface pressure minimum located just southeast of Iceland. Surface observations indicated that the frontal zone had a twin surface front structure, with 100 km between each front (see, e.g., *Browning et al.* [1997, and references therein] for

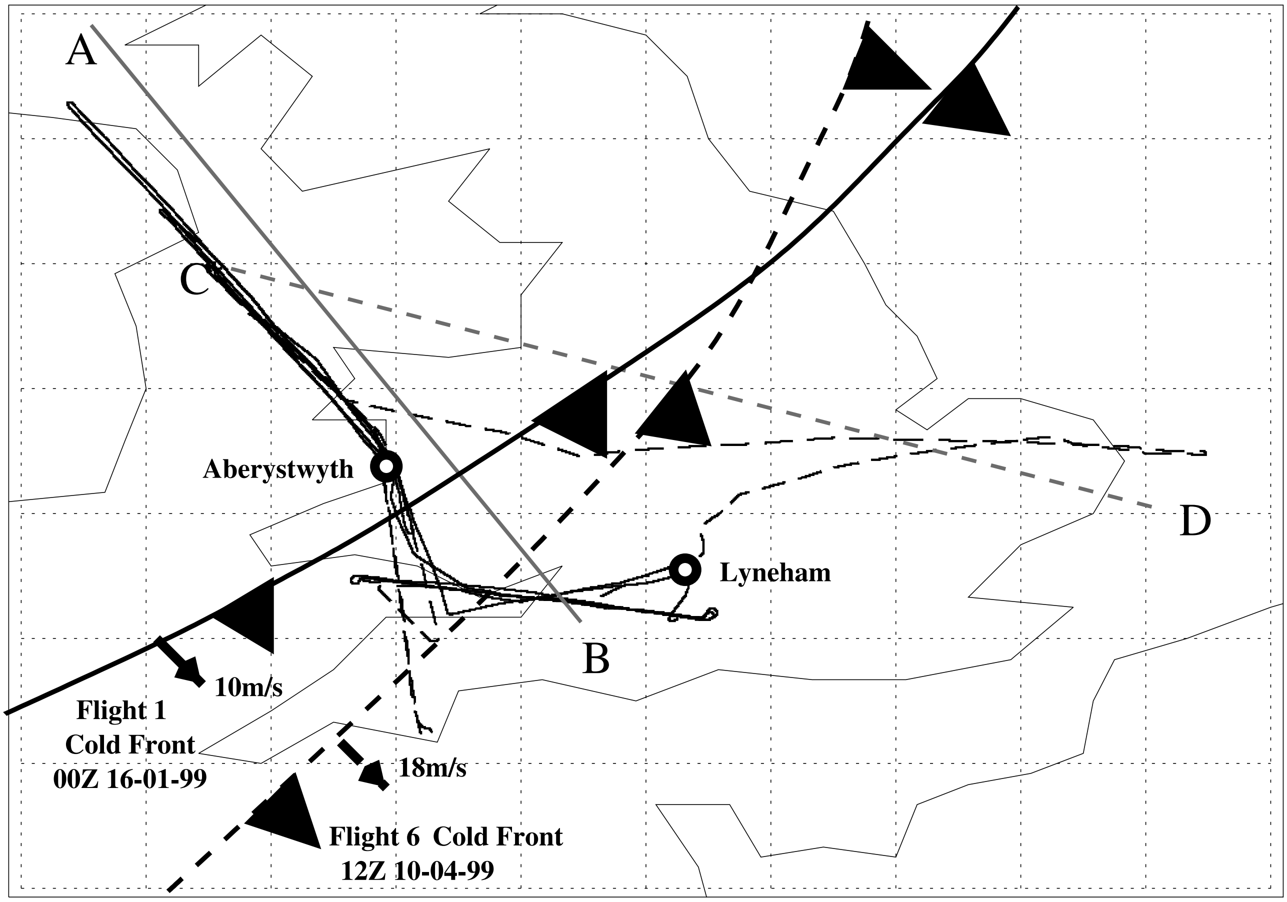

Figure 1. Map showing the flight paths studied by two DCFZ flights. The approximate position and speed of the surface front being investigated during each flight is also marked. The solid curve corresponds to flight 1, the dashed curve to flight 6. The solid straight line AB shows the position of the model cross section used to create Figures 4 and 5, and the dashed straight line CD corresponds to Figures 9 and 10.

a discussion of multiple cold front structures). Surface θ_w was measured to be approximately 288 K in the warm sector, 284–285 K between the two fronts and <280 K behind the cold front. The RDF PV picture reveals that a large intrusion of air previously with elevated PV (>1 PVU, where 1 PVU = 1×10^{-6} K kg^{-1} m^2 s^{-1}) lies just behind and parallel to the surface cold front on the 300 K isentrope. As we shall show in what follows, part of this airmass, the dry intrusion, folds into the frontal zone. This can occur as (downward) advection will be approximately isentropic, and there is a strong gradient in the height of this isentrope in the frontal region. The subsequent development of this synoptic system resembles the cyclonic "P1" events described by *Peters and Waugh* [1996] as the thin filament of low PV tropospheric air stretching from Scandinavia to Iceland is eventually thinned out and apparently mixed into the high PV air.

[10] For flight 6 the synoptic low-pressure system is much weaker with its minimum located just to the north of Scotland. The surface cold front corresponding to this system is weaker than the flight 1 case and is also oriented southwest-northeast over the United Kingdom. This was confirmed by surface measurements of θ_w, which were 283 K ahead of the front and 279 K behind it. The RDF PV picture shows a more complex picture than flight 1. Thin filaments of (ex-)high PV air have been drawn cyclonically around the low-pressure system and into the cold frontal zone. Note that we have used the 310 K isentropic surface in this case because it is located at a similar height in mid-April to the 300 K surface in mid-January. This isentropic surface also slopes in the cold frontal zone, but the slope is weaker compared with the more intense system of flight 1.

3. Data and Analysis Methods

3.1. Flight Measurements

[11] The aircraft instrumentation used in this work is listed in Table 1 together with references for further details. Measurements of NO_x (nitrogen monoxide and nitrogen dioxide) and NO_y (the sum of reactive nitrogen compounds) were only available for the April flight (flight 6), when the DCFZ campaign coincided with the MAXOX (MAXimum OXidation rates in the free troposphere) chemistry experiment. A full description of the instrument fit for the MAXOX experiment is given by *Hov et al.* [2000]. Following, for example, *Bethan et al.* [1998], wet-bulb potential temperature θ_w was calculated from measured true temperature and dew-point temperature using the formula of *Bolton* [1980]. In the

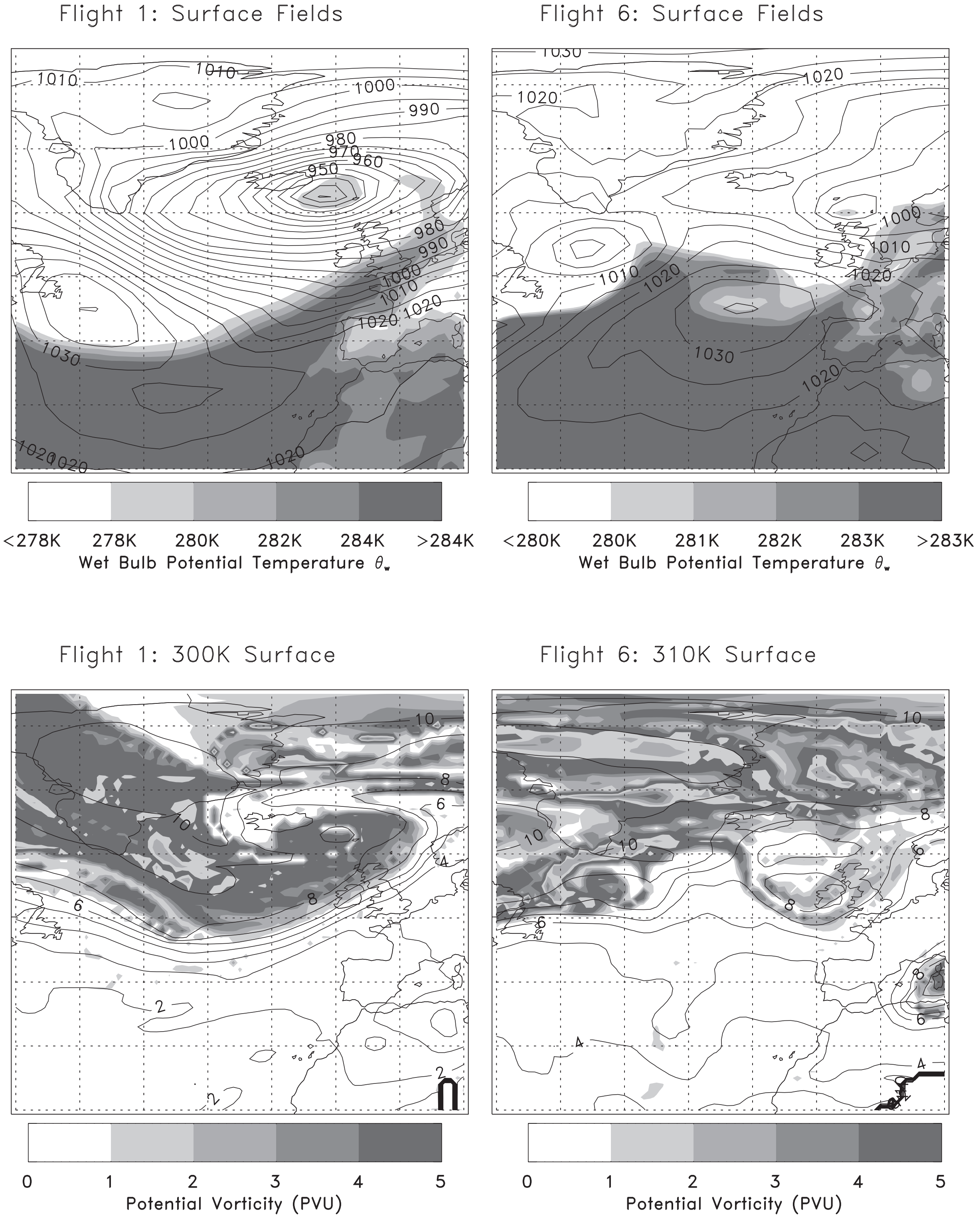

Figure 2. Contour plots illustrating the synoptic situation at the time of the two flights (left-hand panels: 0000Z on 16 January 1999; right-hand panels: 1200Z on 10 April 1999). On the upper panels the solid contours are isobars of sea level pressure (contour interval (c.i.) 5 hPa), and the filled contours are θ_w. In the lower panels the filled regions show the 2.0-day RDF PV field (see text) on the 300 K (flight 1) or 310 K (flight 6) isentrope. The solid contours mark the geopotential height of this isentrope in kilometers.

absence of mixing and external heating, θ_w is conserved in both saturated and unsaturated air, and so is a useful marker of airmass origin. There is a one-to-one correspondence between θ_w and equivalent potential temperature θ_e, which is also often commonly used to identify airmasses [*Emanuel*, 1994], so the choice between them is largely a matter of convention.

[12] As a measurement of turbulence encountered by the aircraft, the variance of w' calculated over a period of 10 s has

Table 1. Details of Measurement Instruments and Techniques on Board the C-130 Hercules Aircraft During DCFZ

Parameter	Methods and Instrumentation	Instrument Accuracy	References or Comments
Temperature	platinum resistance thermometers Rosemount 102AL and 102BL (de-icing heater off for 102BL)	±0.3 K	*Inverarity* [1999a]
pressure	variable capacitance (Rosemount 1201F)	±3 mbar	*Offiler et al.* [1999]
Dew point	thermoelectric hygrometer (General Eastern 1011B)	±0.3 K at 270 K ±1 K at 200 K	can take minutes to equilibrate at <250 K
Total water	Lyman alpha absorption (UKMO developed)	±0.15 g kg^{-1}	*Nicholls et al.* [1990]
Position (latitude, longitude, and altitude)	GPS (Navstar XR5), RADAR altimeter (Honeywell YG9000D1) Kalman filtering used for position accuracy	±50 m	*Inverarity* [1999b] pressure height used above 1500 m
Horizontal wind components	Pitot Static System (Rosemount 1221F) Inertial Navigation unit (Honeywell H423) angle of sideslip vanes (Penny and Giles E23001), GPS (Navstar XR5)	±0.5 m s^{-1}	*Inverarity* [1999b] *Offiler et al.* [1999]
Vertical wind component	Pitot Static System (Rosemount 1221F) Inertial Navigation unit (Honeywell H423) angle of attack vanes (Penny and Giles E23001)	±0.6 m s^{-1}	*Offiler et al.* [1999]
Ozone	UV absorption (Thermo Environmental Instruments Inc., model 49)	Larger of ±3% or ±1 ppbv	*Hov et al.* [2000]
Carbon Monoxide	vacuum UV resonance fluorescence (developed by Forschungszentrum Jülich)	±4%	*Gerbig et al.* [1999] *Hov et al.* [2000]
NO_x/NO_y	chemiluminescence (developed by University of East Anglia)	±21% (NO) ±26% (NO_2) ±25% (NO_y)	*Hov et al.* [2000]

been calculated from the 1-s winds. This quantity will be referred to as $\langle w'^2 \rangle$. The relationship between $\langle w'^2 \rangle$ and the rate of turbulent energy dissipation is discussed by *Weinstock* [1981]. The qualitative picture of turbulence obtained in this way was found not to depend strongly on the variance time interval when chosen in the range 4 s up to about 1–2 mins. This implies that the vertical velocities measured are associated with three-dimensional turbulence rather than the signature of gravity waves.

3.2. Mesoscale Model Data and Trajectory Methodology

[13] The mesoscale model data that have been used to interpret the aircraft measurements consist of 18–30 hour forecasts from the UK Met Office mesoscale model in limited area mode. Back-trajectory calculations are made from the forecast time back to the beginning of the forecast, using the trajectory model of *Wernli* [1997]. The horizontal resolution of the forecast winds is approximately 15 km × 15 km, and the temporal resolution is 1 hour.

[14] Reverse-domain-filling (RDF) back trajectories are released simultaneously from a three-dimensional grid that spans the area of the flight path in the horizontal at 15 × 15 km resolution, and has 21 levels in the vertical from 0–10 km. The back-trajectory calculations cease when parcels leave the model domain, which extends from approximately −16°E to 10°E and 44°N to 60°N. Note that allowance is made for parcels leaving the domain in the origin of air calculations presented in sections 3 and 4. By reconstructing fields of near-conserved quantities like θ_w and PV using RDF, we expect to model measured small-scale features with strong gradients more accurately, compared with the instantaneous model θ_w and PV fields. This is because the RDF fields are not subject to diffusion at the model grid scale. However, the RDF fields do not represent the effects of recent turbulent mixing or diabatic heating, so where these processes are important, RDF quantities will diverge from measured quantities and may be less accurate than instantaneous fields. Discussion of the comparison between observations, instantaneous model θ_w and PV, and reconstructed RDF fields is included in sections 4 and 5.

[15] For each of the cases studied, we found a strong degree of symmetry in the along-front direction in both the mesoscale model meteorological fields and the trajectory results. (Bear in mind that we are concentrating on a region of just a few hundred kilometers square in each case.) For this reason, we have chosen to present our results in the form of cross sections in the cross-front-height plane (see Figure 1). When interpreting these pictures it is helpful to bear in mind that the aircraft flight path does not remain exactly within a single such plane, and that our presentation assumes that along-front variations encountered by the aircraft will also be small. This is one possible reason, distinct from trajectory error or wind field inaccuracy, for differences in the exact positions of features identified by the trajectory analysis and those in the measurements.

[16] The model cross sections presented are from a fixed reference time at some point during the flight. The motion of the front during the flight is accounted for, when comparing aircraft and model data, by defining a relative position of the aircraft relative to the front at the time of each measurement. Constant front speeds (see Figure 1), estimated from sequences of UKMO LAM charts, are assumed in order to calculate the relative position, and a forecast error of 1–2 hours based on surface front arrival time, is also allowed for in each case. This is equivalent to subtracting a constant distance from the relative position, equal to error time × front speed. The flight paths superimposed on the model cross sections in the figures that follow are plotted according to their relative position to the front rather than the absolute position of the aircraft.

[17] To interpret further our results, we have developed the coherent ensemble trajectory method [*Wernli*, 1997;

Wernli and Davies, 1997]. Essentially, this is a method of grouping together backward or forward trajectories that have similar properties. In our case we choose criteria that are relevant to different branches of the observed circulations, such as trajectories with a given rate of ascent or descent, or those with a given value of potential vorticity at a previous time. We have combined this approach with the RDF technique [*Sutton et al.*, 1994] in order to present quantities detailing the Lagrangian history of airmasses on the cross-front cross sections described above.

[18] For the purposes of comparison with the mesoscale trajectories, 4-day global back trajectories were also calculated for the same time intervals and regions using archived winds from ECMWF operational analysis at T106 resolution (approximately 1.125° × 1.125°) (see *Methven et al.* [2001] for details). The temporal resolution of the winds in this case is 6 hours, and the trajectory model used is described by *Methven* [1997]. The global trajectories provide an indication of the origin of air masses prior to entering the mesoscale model domain, albeit with lower wind resolution. In fact, we shall show that the extra information provided by the longer back trajectories is more helpful in interpreting flight measurements than features unique to the mesoscale model that may appear due to higher wind resolution. Reference will be made in sections 4 and 5 to the comparative resolution of features in the global-scale calculations as compared with the mesoscale calculations. In addition, saturation mixing ratios along the 4-day back trajectories are used to infer subsequent mixing of descending air parcels.

4. Flight 1: Cold Front 16 January 1999

[19] Flight 1 of DCFZ took place at night between 2030 and 0230 GMT on 15–16 January 1999 through a cold frontal zone traveling southeastward across the United Kingdom; see Figures 1 and 2 (left-hand panels). Figure 3 shows graphs of quantities measured during the flight against time, along with various quantities calculated from the mesoscale model data. In Figure 3a we can compare measured θ_w with mesoscale model instantaneous and 18-hour reverse-domain-filling RDF θ_w interpolated onto the flight track (using relative position as described above). The RDF θ_w is simply the θ_w of each air parcel 18 hours previously along each trajectory. The agreement between all three curves (allowing for forecast error in the front position as described above) is good, except in the later stages of the flight where the flight path repeatedly crosses one of the twin surface fronts at low levels. The twin surface front structure is not well captured by the mesoscale model. No significant improvement appears to be gained using by the RDF θ_w field instead of the instantaneous field, a result that applies to all flights we have studied in detail.

[20] Measurements of O_3, CO and humidity (specific q, relative $\mathcal{H}$) in Figures 3b and 3c reveal long periods during which near-constant ozone (35–45 ppbv) saturated air has been sampled, with weakly varying CO (100–150 ppbv). This is characteristic of the relatively constant tropospheric background O_3 measured during the photochemically inactive winter season [e.g., *Parrish et al.*, 2000]. The constant measurements are broken only by two thin relatively dry regions, marked A and B, and a 1.5-hour period during which dry air with often greatly elevated ozone levels was measured (C to H).

[21] Figure 4 shows cross sections of model data (mesoscale model θ_w, q, and PV, and global model 1.5-day RDF PV) with the aircraft flight path, relative to the surface front position, interpolated onto the same cross section. Note that the thickness of the flight paths in Figures 4 and 5 varies with measured quantities (see captions), and letters labeling peaks and layers in the measurements in Figure 3 have been added to make it easy to detect the relative location of measured features. Also, because of the noisy (grid-scale) nature of mesoscale model PV, the PV field in Figure 4c has been averaged in time along trajectories for 12 hours. This process creates a smoother field which we believe is both more dynamically relevant and a better indicator of origin of air. In Figure 4a the surface front, defined by a strong horizontal gradient in θ_w, is located near the edge of the model cross section at 600 km. However, the details of the observed twin structure of the surface front are not visible in the mesoscale model fields. At upper levels, the front lies to the northwest of the surface front, and is located at the 6-km (450 mbar) level at 0 km on our cross section. The q cross section (Figure 4b) is dominated as might be expected by a strong vertical gradient, but there is also a strong horizontal gradient in a region that coincides only approximately with the upper level front. The mesoscale PV cross section (Figure 4c) reveals a lowered tropopause at 300–600 km behind the surface front(s), and an intrusion of elevated PV lying along the front at upper levels. There is also a region of elevated PV ahead of the surface front, and this seems likely to be of low-level origin and to have been generated by diabatic effects, as it is in a region of ascending air. A similar low-level PV anomaly ahead of a cold front is described by *Browning and Golding* [1995]. The global trajectory −1.5 days RDF PV (Figure 4d) shows a similar PV intrusion along the upper level front as in Figure 4b. In addition, there is a high PV feature at low level (300 km, 900 mbar) and some evidence for a small tropopause fold at 450 km, 300 mbar.

[22] Figure 5 shows some Lagrangian properties of the air parcels as calculated from the mesoscale trajectories. Figure 5a is a contour plot of the rate of change in log-pressure height, calculated over the previous 18 hours or from the time when each parcel enters the domain, whichever is the more recent. The picture is dominated by a region of uplift ahead of the front, extending from the surface to the tropopause, with a width of around 200–300 km. The maximum uplift is located directly above the surface front at around 400 mbar. Air behind the surface front is descending, with the most rapid descent taking place just below the PV intrusion. The air in the PV intrusion itself is moving on a relatively level trajectory. Figure 5b shows the direction of origin of the air in degrees (i.e., 0° indicates from the north and 180° from the south). The striking feature in this plot is the sharp gradient of 30° in origin at the surface front, with the air behind originating in the west (270°), and the air ahead originating from the southwest (240°), within the warm sector.

4.1. Dry Intrusion

[23] From Figures 4a, 4c, and 4d, it is immediately clear that a dry layer including the measurements labeled G-F-D-E, B and A extends downwards roughly coincident with the PV intrusion present in both the mesoscale model and the

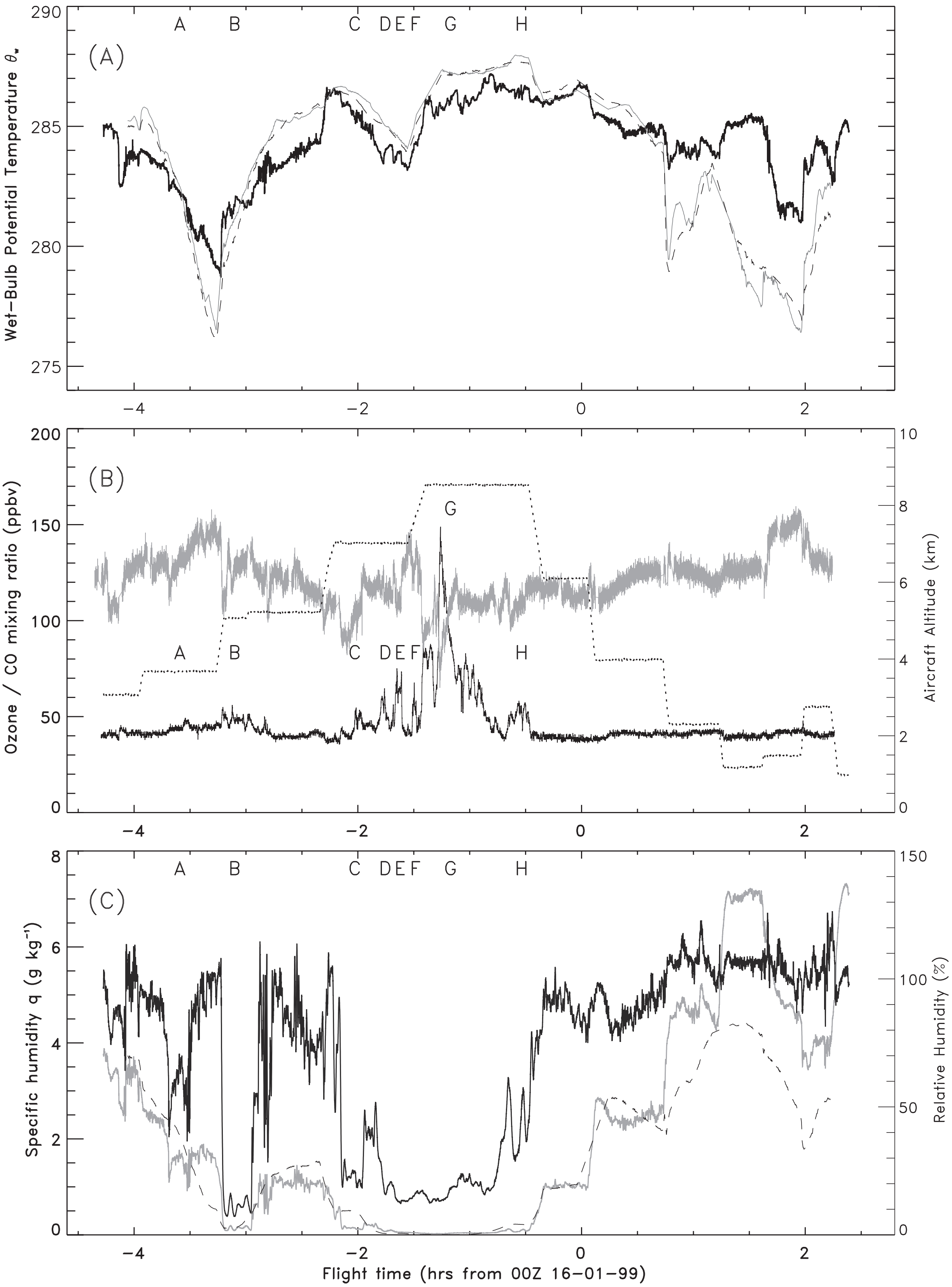

Figure 3. Measurements made during flight 1 on 16 January 1999. (a) Wet-bulb potential temperature θ_w (solid curve). The dashed black curve is the model θ_w interpolated unto the flight path and the shaded curve is the RDF model θ_w (see text). (b) Ozone (black curve) and carbon monoxide (shaded curve). The dotted curve shows aircraft altitude above sea level. (c) Specific humidity q in g kg^{-1} (shaded curve). The dashed black curve is the model q, and the solid black curve is relative humidity $\mathcal{H}$.

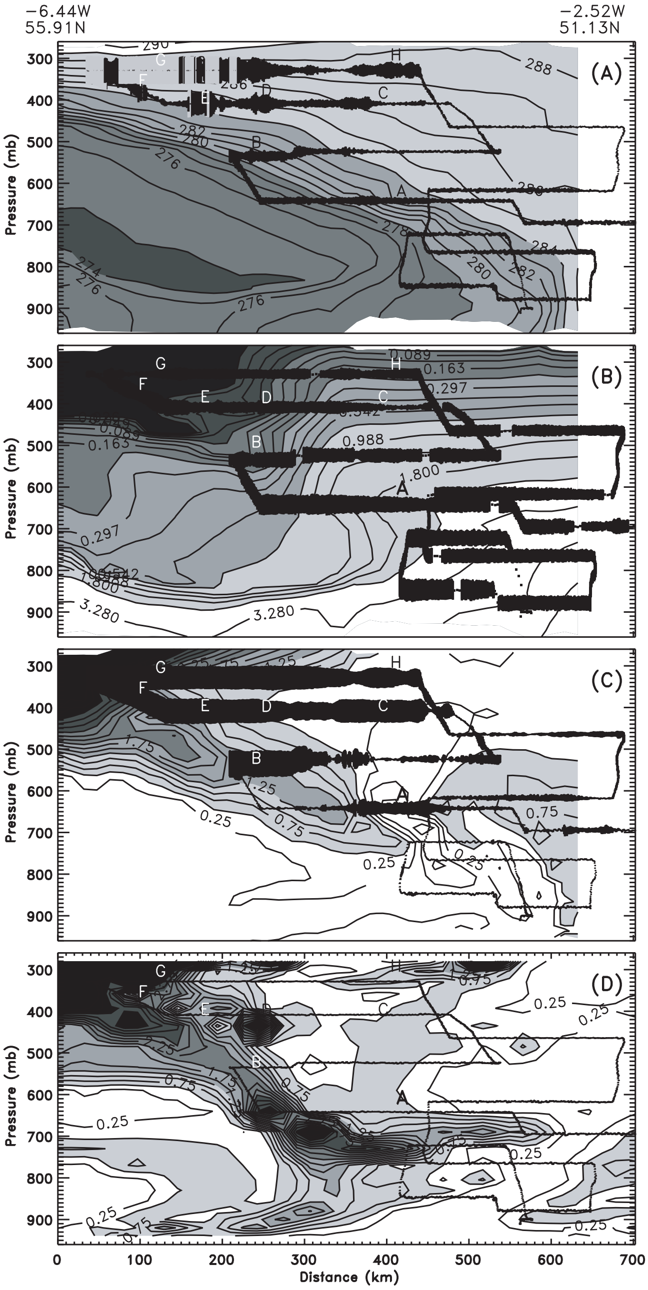

Figure 4. Contour plots showing mesoscale model forecast fields along a cross section through the cold frontal zone close to the flight path. The flight path relative to this cross section is plotted onto each panel. (a) Model θ_w, c.i. 1 K. (b) Specific humidity q (in g kg^{-1}). (c) Mesoscale model PV, averaged along back trajectories for 12 hours (or until the parcel leaves the model domain), c.i. 0.25 PVU. (d) Global trajectory −1.5-day RDF PV. The thickness of each flight path curve is proportional to (Figure 4a) [O$_3$]-38 ppbv, except values above 70 ppbv marked as shaded (Figure 4b) [CO]-80 ppbv, and (Figure 4c) 100%- relative humidity (in %).

global RDF trajectories. The dry layer includes two thin layers of enhanced ozone, with the peaks at D and E, and there is also enhanced ozone relative to the background level at B (3–10 ppbv with several peaks) and A (1–5 ppbv in thin layers). This evidence strongly indicates that the G-F-D-E-B-A feature is the dry intrusion airmass in this frontal circulation (compare Plate 1 of *Grant et al.* [2000]). Another dry, relatively ozone-rich feature has been intersected by the aircraft at both C and H. It does not seem to correspond to any mesoscale model feature, but does appear to correspond to a high PV feature in the −1.5-day RDF PV field in the global trajectory model. Both the ozone and RDF PV in the C-H feature are lower than in the G-F-D-E-B-A dry intrusion feature. The C-H region is separated from the main part of the dry intrusion by a relatively moist region. Ahead of C-H the region of rapid uplift shown in Figure 5a is clearly the warm conveyor belt branch of the frontal circulation discussed below.

[24] Below we will consider the extent of the dilution experienced by descending air in the dry intrusion. If we make the assumption that the high ozone features in the measurements have trajectories similar to the nearest high RDF PV features in the global trajectory field, then the trajectory analysis indicates a similar origin in the lower stratosphere (1.5–3 PVU) for the air encountered at G, F, D, E, B and A. We assume that this lower stratospheric air originally has negatively correlated ozone and CO similar to that measured at G during the highest intersection of the dry intrusion. *Fischer et al.* [2000] demonstrate that a compact

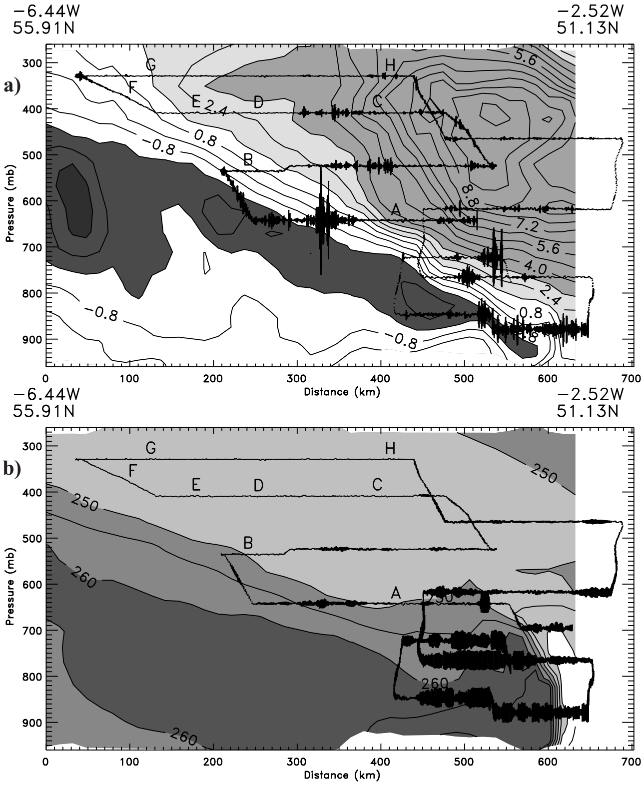

Figure 5. Contour plots giving details of the origin of air as calculated from the mesoscale model back trajectories. (a) Rate of change of pressure-height along trajectories, in km day^{-1} c.i. 0.8. (b) Direction of origin of air in degrees measured clockwise from north, c.i. 5°. In Figure 5a the flight thickness is proportional to the 0.1 s^{-1} variance in w'^2, and in Figure 5b it is proportional to $r_T - r$, a measure of precipitation.

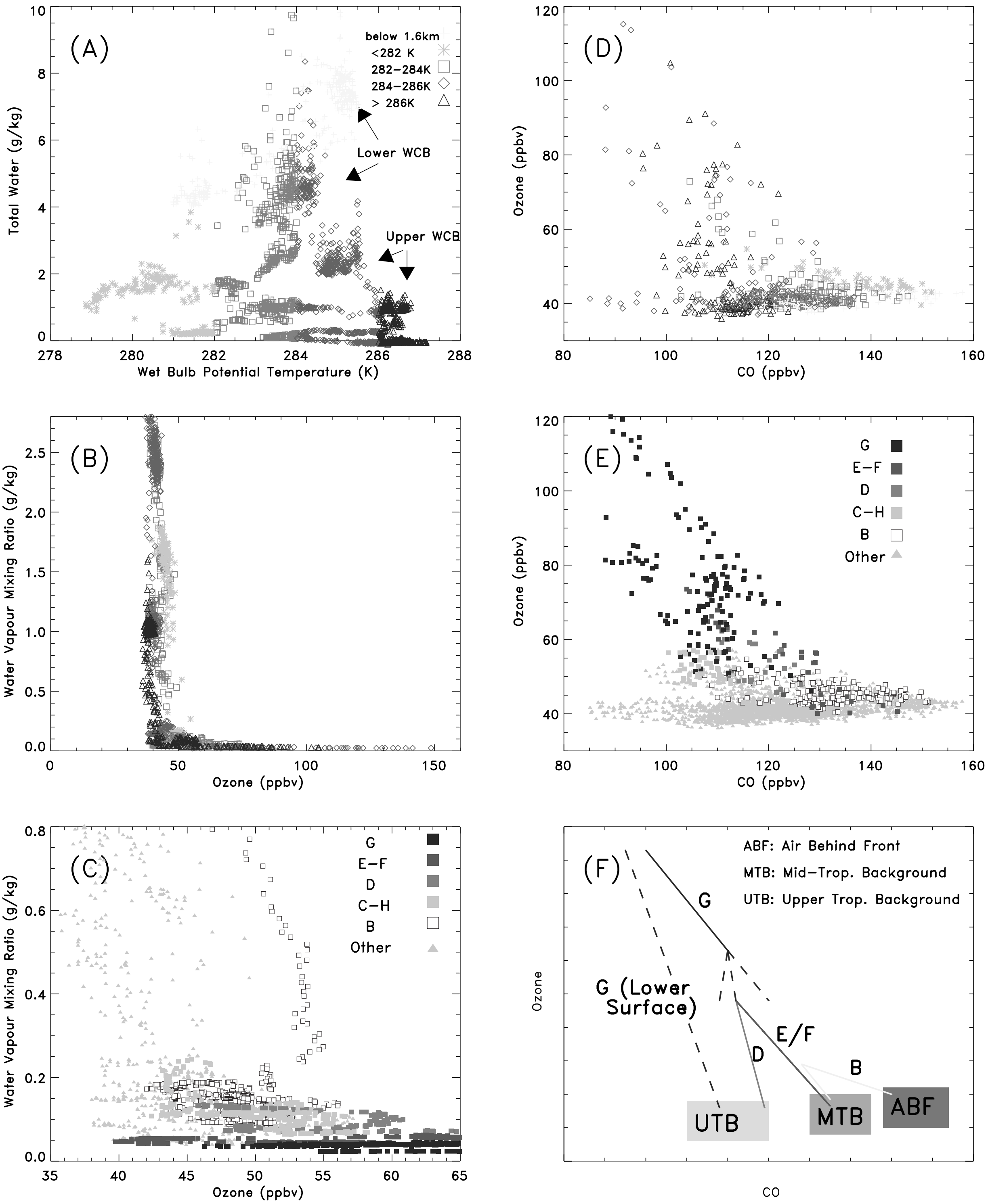

Figure 6. Tracer-tracer scatterplots of measurements made during flight 1. (a) Total water r_T:θ_w. (b) Water vapor mixing ratio r:Ozone, with parcels colored according to their measured θ_w. Parcels are plotted with temporal resolution 30 s. (c) As in Figure 6b but with parcels from the labeled features colored. A higher temporal resolution (10 s) is used. The dotted lines show mixing lines at measurement B. (d) O_3:CO with parcels colored according to their measured θ_w. (e) O_3:CO with parcels colored according to feature. (f) A schematic showing mixing effects in the O_3:CO plot; see text for details. See color version of this figure at back of this issue.

relationship between O_3 and CO typically exists in the lowermost stratosphere. Because of the long chemical timescales of O_3 and CO in winter, deviations from the original relationship encountered at G are best explained by mixing with tropospheric air. Similarly, initial water vapor mixing ratios may be bounded above (see discussion below), so increases in water vapor mixing ratios in the dry intrusion may be explained by mixing with moist tropospheric air.

[25] Figure 6 shows scatterplots of measured thermodynamic and tracer quantities. These include total water r_T and water vapor mixing ratio $r = q/(1 - q)$, both of which mix linearly in unsaturated air. r_T also mixes linearly in air containing suspended liquid water and ice. Points are colored according to their measured θ_w in order that the position of the measurement relative to the front may be inferred. Measurements made below 1.6 km are colored red. Figure 6a shows r_T against θ_w, and will be discussed further below in the context of the warm conveyor belt. Figure 6b shows the r:O_3 scatterplot. This diagram gives considerable insight into the mixing history of the air sampled at different locations within the dry intrusion. Upper tropospheric or stratospheric air with enhanced ozone and low water vapor lies on the horizontal branch of the L-shaped scatterplot, and middle and lower tropospheric air with background ozone and high water vapor lies on the vertical branch. As air descends in the dry intrusion, it approximately conserves its water vapor and ozone mixing ratios in the absence of mixing. If it is mixed and diluted, however, this will be revealed as mixing lines on the scatterplot [e. g., *Plumb and Ko*, 1992]. Mixing of dry ozone-rich air with moist air is of interest chemically as it could lead to locally enhanced OH levels [*Esler et al.*, 2001]. Figure 6c shows high temporal resolution (10 s) data colored differently for each sample of enhanced ozone air. It is clear that at location B in particular, mixing lines (dotted lines) have formed with moister air. There are in fact two such lines, corresponding to mixing on the lower surface of the dry intrusion with moist air behind the front, and on the upper surface with background upper tropospheric air on the fringe of the WCB. Similar arguments can be made for mixing at C-H and D, but there is no evidence of mixing at G or E-F. This means that mixing has not taken place with moist air at these locations, although mixing with another dry airmass is still a possibility.

[26] Figures 6d and 6e show the O_3:CO scatterplot. In Figure 6d the points are colored according to their measured θ_w as in Figure 6b. The samples taken from behind the front (orange stars with $\theta_w < 282$ K) have slightly higher ozone (45 ppbv) and higher CO (140 ppbv) compared with air ahead of the front (cyan diamonds and blue triangles, $[O_3] = 40$ ppbv, $[CO] = 100-130$ ppbv). Air measured in the upper troposphere with the highest θ_w (blue triangles, $\theta_w > 286$ K) has the lowest CO (100–110 ppbv). The points with greatly enhanced ozone are all samples from either the dry intrusion (G-F-E-D-B-A) or the other dry, enhanced ozone feature encountered at C-H. In Figure 6e, measurements from these features are shown at higher temporal resolution, using the same color coding system as in Figure 6c.Note that similar CO and ozone have been recorded at C and H, supporting the earlier hypothesis that the flight has intersected the same filamental structure at these two locations.

[27] Figure 6f is a schematic presenting our interpretation of how dilution of the dry intrusion manifests itself on the O_3:CO scatterplot shown in Figure 6e as mixing between the dry intrusion air and different reservoirs of background air takes place. For schematic purposes the dilution of the dry intrusion as it descends is represented by single mixing lines, although in reality mixing of the background air into the dry intrusion is likely to be a more continuous, ongoing process. The characteristic O_3:CO ratio at G, the highest intersection of the dry intrusion (8.5 km), is shown by the solid blue line. However it is notable that air on the lower surface of the intrusion at G lies off this relationship on the dashed blue curve. This can be accounted for if mixing has taken place between the dry intrusion and upper tropospheric background air (UTB), and the dashed blue line is interpreted as a mixing line between undiluted dry intrusion air and UTB air. At 7.1 km the intersections of the dry intrusion include D, E and F, the dry intrusion appears to have already been greatly diluted by background air. Differences in the O_3:CO ratios can be explained if the air at D, on the upper surface of the intrusion, has been mixing with UTB air (green line), whereas the air at E and F on the lower surface has mixed with the mid-tropospheric background (MTB) air below the intrusion at this level (cyan line). Similarly, looking at the red lines, air on the upper surface of the intrusion at B mixes with MTB air, and on its lower surface it mixes with air from behind the front (ABF) that has distinctly higher CO and O_3. Mixing on both the upper and lower surfaces of the dry airmass accounts for the 25 ppbv gradient in CO concentrations measured at B.

[28] A more detailed analysis of trajectory histories from the global trajectory model calculations can provide further evidence of mixing. Table 2 shows previous temperatures recorded along back trajectories, along with the saturation mixing ratios of water vapor with respect to ice at those temperatures, at various locations along the dry intrusion and also in the C H feature. Also given in Table 2 is the measured water vapor content at those locations. It is clear that the measured water vapor content is very much greater than the previous saturation mixing ratios. Possible explanations for this are (1) precipitation has fallen from a saturated layer above the air parcel as it descended, and then evaporated in the parcel; (2) ice particles were present in the air parcel throughout its descent which then evaporated as the temperature rose; or (3) the air parcel has been mixed with and diluted by moist air as it has descended. Possibility 1 may be eliminated, except at A, as above the descending dry intrusion at B-D-E and C-H both models and measurements indicate only unsaturated air. Concerning possibility 2, an upper bound estimate for the number of particles in a typical extratropical cirrus cloud is around 1000 per liter [*Ström and Heintzenberg*, 1994]. At this number density, to store enough water in the cirrus cloud so that it evaporates to produce 10 ppmv of water vapor would require the cirrus particles to previously have had a scale of approximately 20 μm (calculated at 300 mbar and 215 K). Such particles would have terminal velocities of the order of 0.1 ms^{-1}, and so would fall out over the few days that the air parcel is in the stratosphere. This provides more evidence for mixing at E, D, and B, (possibility 3), especially when considered in conjunction with the mixing line evidence presented above, both in the H_2O:O_3 plot and in the O_3:CO plot. Further support is given by aircraft measurements of turbulence (Figure 5a). Intense turbulence

Table 2. Water Vapor Content Compared With Previous Saturation Mixing Ratios Encountered by Typical Dry Intrusion Back Trajectories, Starting Near Measurements Made at A, B, D–E, and H[a]

Sampled Region	Minimum Saturation Mixing Ratio (Ice)	Days −4 to −2.5 Maximum Saturation Mixing Ratio (Ice)	Measured Mixing Frac. Mixing Ratio *r*
A	23.1 (215 K, 393 mbar)	50.8	1200–1700
B	14.8 (211 K, 335 mbar)	40.2	200–250
D–E	19.7 (213 K, 313 mbar)	77.2	100–150
H	23.5 (212 K, 219 mbar)	81.4	150–200

[a] Water vapor mixing ratios are in units of 10^{-3}g kg^{-1}.

and precipitation (see Figure 5) was encountered just below the dry intrusion at B and A, in a region consistent with slantwise convection (see the schematic Figure 8.8 of *Browning* [1990]). Patches of intermittent moderate turbulence were also encountered throughout the dry intrusion region.

[29] This apparent mixing of the dry intrusion illustrates that this intense cyclonic system need not necessarily efficiently transport air with an upper tropospheric or stratospheric signature to the lower troposphere, at least not without significant dilution taking place.

4.2. Warm Conveyor Belt

[30] *Browning* [1990] describes the WCB region as being archetypally characterized by a narrow cold frontal rainband at the surface front, where there is line convection, embedded within a wide cold frontal rainband undergoing slantwise ascent. From the chemical transport perspective, interesting questions concerning the warm conveyor belt include the extent to which ascending middle to upper tropospheric WCB air is mixed with lower tropospheric air. For example, to what height is the WCB ventilated by line convection from the narrow rainband above the surface front? Does turbulent mixing within the WCB result in a relatively homogeneous airmass, or is the WCB sufficiently stably stratified to inhibit vertical mixing? Could such stratification then result in the WCB containing several layers of distinct origin and chemical signature? These questions are particularly relevant to instances where the WCB transports polluted air from the eastern seaboard of the United States [*Parrish et al.*, 2000] or Asia. Plumes of high NO_x that appear to be associated with WCB transport from the polluted boundary layer have been reported [*Brunner et al.*, 1998]. The rate of mixing of parcels of polluted air entering the free troposphere has been shown to be an important factor affecting trace gas concentrations [*Wild et al.*, 1996]. As WCB trajectories typically move parallel to the surface cold front [e.g., *Browning*, 1990], WCB air sampled over the United Kingdom is more likely to contain air of marine origin than recently polluted air, although layers of ex-WCB polluted air from previous systems may be encountered [*Stohl and Trickl*, 1999].

[31] The sonde and aircraft observations made during DCFZ go some way to answering the above questions, at least for this case study of the WCB along the cold front of a mature cyclonic system. (This contrasts with the synoptic situation of a developing baroclinic wave studied by *Bethan et al.* [1998, section 3.6].) The flight 1 WCB contains marine air of fairly uniform chemical signature, with higher ozone (35–45 ppbv) compared with the four marine boundary layer WCB airmasses recently studied by *Grant et al.* [2000] as part of the NASA Subsonic Assessment, Ozone and Nitrogen Oxide Experiment (SONEX) (lowest values 18–22 ppbv).The higher levels of ozone may be explained by the lower level of photochemical activity, and hence lower rate of ozone loss in the marine boundary layer, in January compared with October when the SONEX measurements were taken. In addition, the SONEX marine boundary layer WCBs were of eastern Pacific origin, where air may have a longer marine boundary layer residence time compared with the central Atlantic origin in this case.

[32] In Figure 5, the WCB trajectories are seen to be defined by an airstream that is rapidly ascending from the southwest. The airstream is also characterized by enhanced wind speeds along the front. The air that has recently experienced the most rapid uplift is at height 7 km (400 mbar) and relative position 550 km, just behind the second of the twin surface fronts. The ascent rate here is 6 km over 18 hours (after which time the back trajectories leave the model domain). The global trajectories (not shown) have lower uplift rates, presumably due to the coarser resolution of the wind fields, but these confirm that the WCB jet extends out to the 800 km position, 100–150 km ahead of the first surface front. Most WCB parcels were found to leave the boundary layer (taken to be the nearest 1 km to the surface) in the mid-Atlantic between 20° and 35°N.

[33] Figure 7 shows ozone sonde measurements made during flight 1 along with measurements from the short aircraft profiles made within the WCB. WCB air was identified both by physical and chemical measurements and by the calculated relative position of the measurements to the surface fronts. Two of the three ozone sondes were launched from Aberystwyth before the arrival of the twin surface fronts, passing through ascending, saturated WCB air at approximate relative positions 790 km and 660 km, respectively; that is, the first sonde was launched about 100–150 km ahead of the surface front, and the second was launched shortly before the arrival of the first surface front at Aberystwyth. The profiles give a contrasting picture of the WCB depending on their relative positions to the surface fronts. Sonde 1 passed through low-level warm sector air up to 750 mbar (2 km), before meeting a unsaturated layer (relative humidity $\mathcal{H}$ = 90–95%) at 750–650 mbar (2–3.2 km) that marks the lower boundary of the WCB. Above this, the positive gradient with height in the θ_w profile shows that the WCB in this region is stably stratified. Ozone values are 36–42 ppbv with a high variance in the measurements. The aircraft profile at 680 km (taken at 0030Z at −1.5E, 51.2N, and indicated by the triangles on sonde 1 picture) has encountered very similar air, albeit with lower θ_w by about 1 K. Sonde 2 (at 660 km,

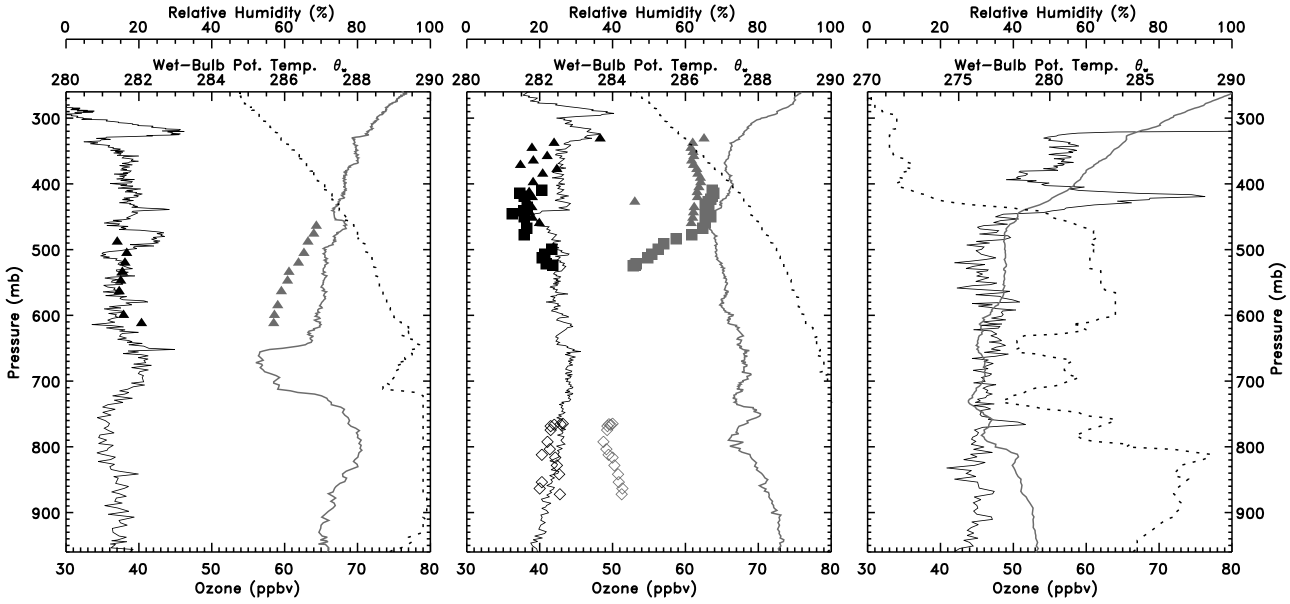

Sonde 1: −11.6hrs (790 km)

Sonde 2: −7.3hrs (620 km)

Sonde 3: 17.2hrs (−90 km)

Figure 7. Ozone sonde measurements made from Aberystwyth around the time of flight 1 on January 15 and 16, 1999. Quantities plotted are ozone (solid black curves), θ_w (shaded curves) and relative humidity with respect to water (dotted black curves). Also plotted are measurements from flight cross sections (see text for details). Note that although the relative humidity is less than 100% above the 600-mbar level in the sonde 1 and 2 measurements, the air is in fact still saturated, but with respect to ice rather than water.

but launched ahead of the first surface front) shows air with a negative vertical gradient of θ_w up to 450 mbar (6 km). The ozone measurements (40–45 ppbv) have low variance suggestive of strong vertical mixing in this region. Aircraft profiles were taken at relative positions behind the surface fronts at 450–500 km (squares: −3.97E, 52.1N, −2.3 hours ≡ 2140Z; triangles: −4E, 52.06N, −0.3 hours ≡ 2340Z). The θ_w profiles indicate that the WCB is stratified and with high variance in ozone at 530–400 mbar (4.5–6.5 km) in this region. A further profile between the two surface fronts at relative position 650 km and height 880–780 mbar (0.5–1.7 km), (diamonds: −1.5E, 51.2N, +1.2 hours ≡ 0120Z) measures ozone to be similar at this level (40–42 ppbv) to that measured by the sonde ahead of both fronts. This is in contrast to the situation shown in Figure 6d, where there is a 3–4 ppbv gradient in ozone across the front.

[34] Combining the *Browning* [1990] archetypal model of the WCB with the above data, the picture that emerges of this WCB in the mid-to-upper troposphere is that of a 200–300 km band of slantwise ascending air (the wide frontal rainband). Stable stratification, and large variance in the vertical of measured ozone, suggests relatively weak vertical mixing and long-range, layerwise motion of tracers. The stable stratification is consistent with the diabatically generated PV within the WCB [*Browning and Golding*, 1995]; see Figure 4c. The exception to this picture is in the region above the first surface front in the narrow frontal rainband (as measured by sonde 2), where line convection appears to penetrate to a height of 6 km or above, smoothing out vertical tracer gradients and resulting in neutral stratification. The WCB may therefore be ventilated by tracers from the planetary boundary layer in this region.

5. Flight 6: Cold Front 10 April 1999

[35] Flight 6 took place on 10 April 1999 between 0900 and 1500 GMT, and explored the cold frontal zone associated with a northeast-southwest oriented surface front. As described above, more chemical measurements were available on this flight as it was joint with the EU MAXOX (Maximum Oxidation in the Free Troposphere) campaign. Figure 2 (right-hand panels) shows the synoptic situation at the time of the flight.

[36] Figures 8–10 can be compared with Figures 3–5 for flight 1, and reveal several interesting differences as well as similarities between the two cold frontal zones. Figure 8 shows measured quantities plotted against flight time as in Figure 3, but with an extra panel showing NO_x and NO_y

Figure 8. (opposite) As in Figure 3 but for flight 6 through the cold front of 10 April 1999. (a) Measured and model θ_w, as in Figure 3 as well as (dotted curve) aircraft altitude. (b) Ozone (black curve) and CO (shaded curve). (c) Relative humidity (black curve), measured specific humidity q (shaded curve), and model q (dashed black curve). (d) NO_y (black curve) and NO_x (shaded curve). The peaks labeled 1 and 2 correspond to boundary layer measurements with (1) $[NO_x] = 31.3$ ppbv, $[NO_y] = 48.8$ ppbv and (2) $[NO_x] = 9.5$ ppbv, $[NO_y] = 15.5$ ppbv.

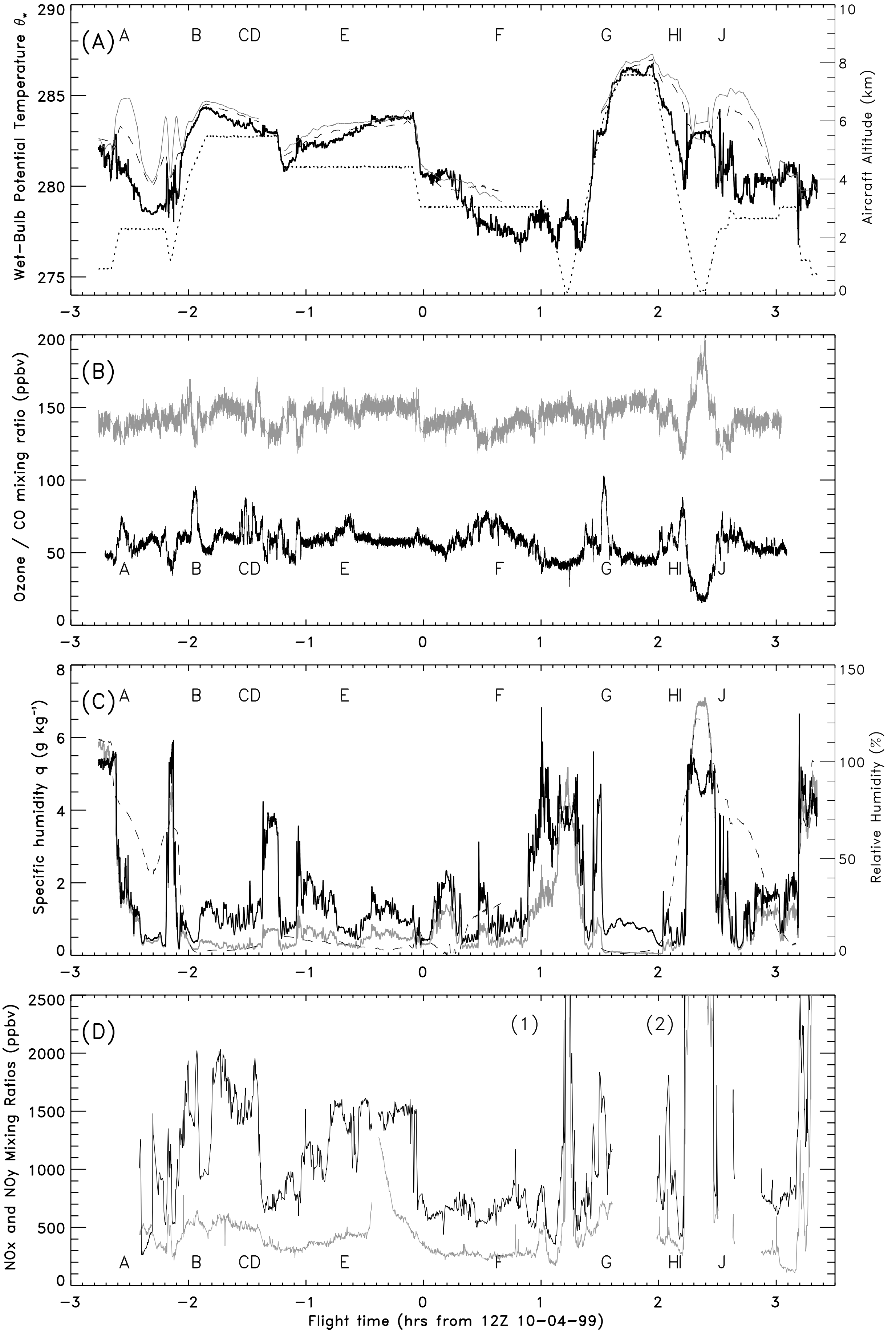
(A)
A
B
CD
E
F
G
HI
J
Wet-Bulb Potential Temperature θw
Aircraft Altitude (km)
290
285
280
275
10
8
6
4
2
0
−3
−2
−1
0
1
2
3
(B)
Ozone / CO mixing ratio (ppbv)
200
150
100
50
0
(C)
Specific humidity q (g kg⁻¹)
Relative Humidity (%)
8
6
4
2
0
150
100
50
0
(D)
(1)
(2)
NOx and NOy Mixing Ratios (ppbv)
2500
2000
1500
1000
500
0
Flight time (hrs from 12Z 10-04-99)

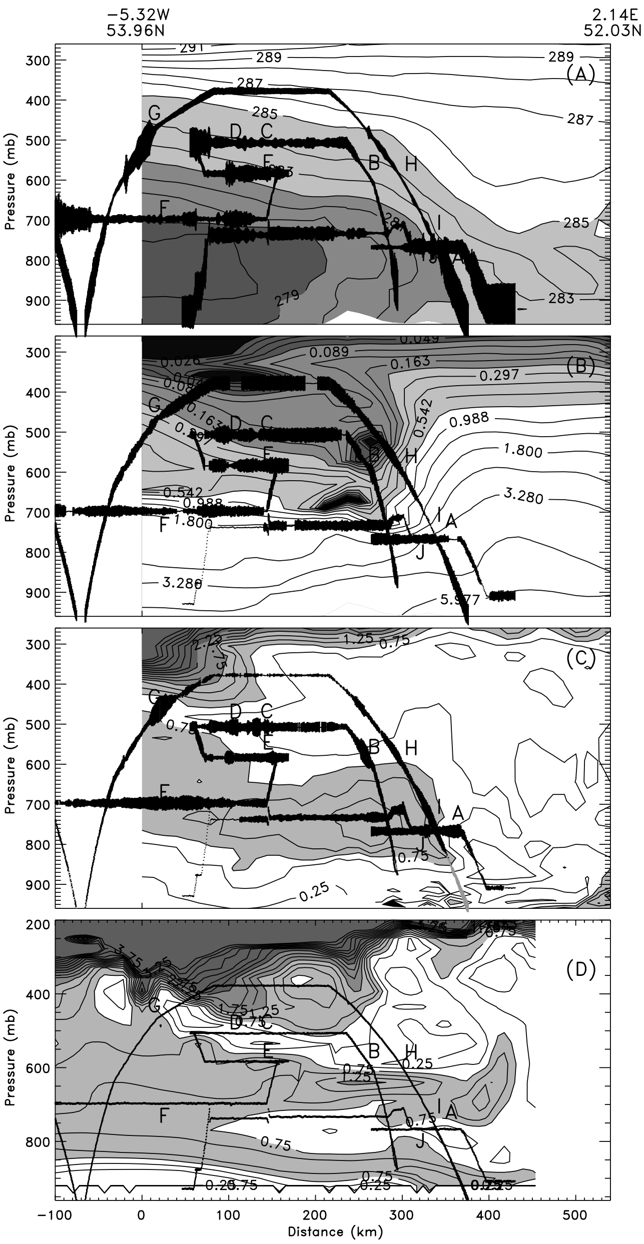

Figure 9. Cross sections of model fields as in Figure 4 but for flight 6: (a) θ_w (c.i. 1 K), (b) q (g kg^{-1}), (c) mesoscale model PV (c.i. 0.25 PVU), and (d) global model −1.5 days RDF PV. The flight path thicknesses are proportional to (Figure 9a) relative humidity $\mathcal{H}$, (Figure 9b) [CO] −120 ppbv, (Figure 9c) [O_3] −40 ppbv (shading corresponds to [O_3] <40 ppbv), and (Figure 9d) flight path only; see text for details.

measurements during the flight. To aid interpretation as before, 10 local peaks in ozone have been labeled A–J that are also plotted on cross-sections in Figures 9 and 10 (see captions for details of line thicknesses). Comparing the mesoscale model forecast and measurements it can be seen that the model again provides a reasonably accurate forecast of θ_w, but a much less accurate forecast of q, as most thin layers are not resolved. From Figure 9 the surface front is located between 300 and 400 km in the mesoscale model θ_w cross section, and behind it there is an upper level front at height 2.7–4 km (600–700 mbar) that slopes upwards away from the surface front with an aspect ratio of 250:1. In Figure 10b the front can also be observed as a gradient in the direction of origin of the air parcels, with a difference of about 20° in origin between warm sector air and air behind the cold front. As with flight 1, the measurements reveal that flight 6 passed through a dry intrusion region above the surface front, including all of the flight path above the surface demarcated by G-D-C-(E)-I. Above 4 km (600 mbar) there are local peaks in ozone, and minima in CO,

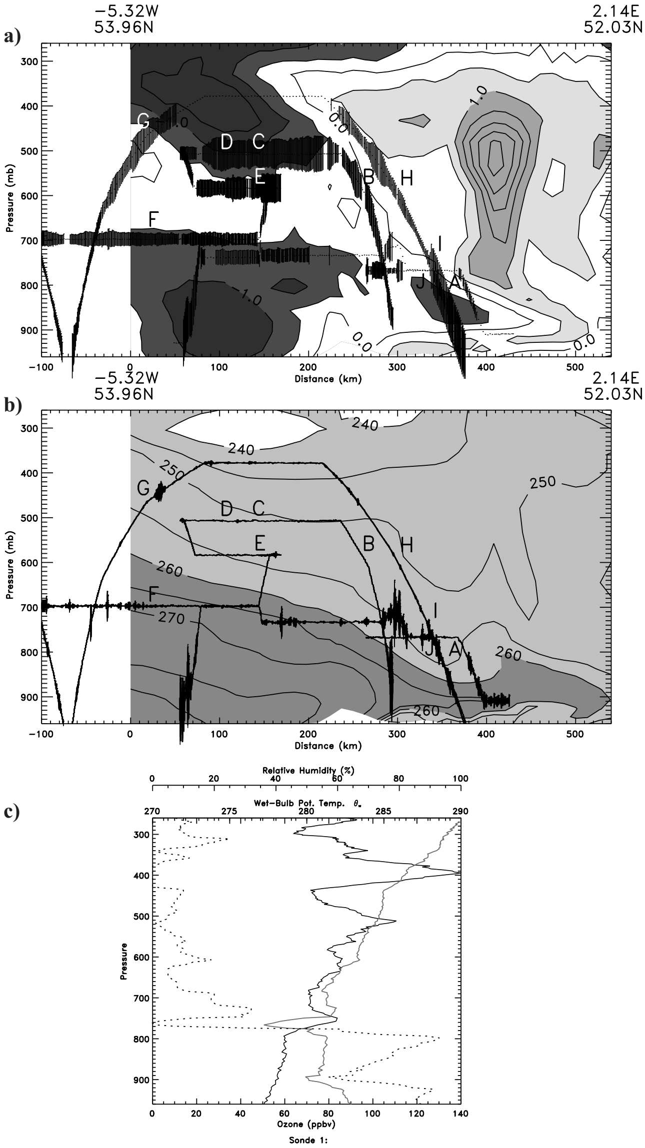

Figure 10. Origin of air as in Figure 5 but for flight 6. (a) Rate of change of pressure-height along trajectories, in km day^{-1} c.i. 0.5. (b) Direction of origin of air, c.i. 5°. In Figure 10a the flight path thickness is proportional to [NO_y], and in Figure 10b it is proportional to the high-frequency variance in w'^2. (c) Aberystwyth ozone sonde for this flight, showing ozone (solid black curve), θ_w (shaded curve) and relative humidity with respect to water (dotted black curve).

at G, D, C, E, B and H which lie in a plane roughly parallel to the upper level front.

5.1. Dry Intrusion and Layered Structure

[37] In Figure 9, there is a contrast between the mesoscale model PV (Figure 9c) and the global model -1.5-day RDF PV (Figure 9d). The latter has a detailed layered structure, with two separate (formerly) high PV sheets lying just above and below the upper level front. The tropopause, as defined by the PV > 2 PVU surface located between 7 and 10 km (400–250 mbar), also appears to be folded in several locations. This structure is reminiscent of the three-dimensional multiple layered structure of stratospheric intrusions described by *Bithell et al.* [1999] (compare in particular their Figures 6 and 7). The mesoscale model PV, by contrast, shows a single thick layer of elevated PV air lying along the upper level front, and a much simpler tropopause structure. This is similar to the global model instantaneous PV field (not shown). For this flight we will show that the global model RDF PV field in Figure 9d is a better guide to the frontal structure compared with the mesoscale model PV in Figure 9c. This may be because, in the absence of mixing, the global model RDF field contains more information about the upper tropospheric/stratospheric origin of each airmass. Instantaneous PV can be strongly influenced by recent diabatic or mixing effects present in both the mesoscale and global model.

[38] Comparing the flight measurements with Figure 9d, it can be argued that the enhanced ozone feature G-D-C-E-B-H corresponds to the layer of enhanced RDF PV (0.5–1.25 PVU) lying just above the upper level front. The PV feature is at a slightly lower level compared to the measured feature, but apart from trajectory error, this could be due to the three-dimensional aircraft path not corresponding exactly to the cross section shown (see Figure 1). Similarly, the high ozone measured at A, I, and J can be associated with the lower layer of enhanced PV, and the broad layer of enhanced ozone at F with another intersection of this lower layer. The correspondence between enhanced ozone and high RDF PV is not exact, however, as the aircraft does not meet enhanced ozone after passing point G, despite appearing to cross air with stratospheric values of RDF PV. However, the RDF PV features all lie 0.5–1 km below the enhanced ozone features, so it seems possible that in reality the aircraft passed just beneath the high ozone-high PV region during this leg of the flight.

[39] The layered structure is seen especially clearly in the ozone sonde shown in Figure 10. It was launched from Aberystwyth at 0920Z, just before the flight, and on our cross section it is calculated to be at a relative position of 260 km, i.e., about 100 km behind the surface front. Major peaks in ozone are present at 2.4 km (770 mbar), 5.4 km (500 mbar), and 7.3 km (400 mbar). The first of these peaks can be associated with the lowermost enhanced PV layer, and is at the same height as the aircraft measurements of enhanced ozone at A, I and J. The second peak is at a comparable height to the G-D-C-E-B-H feature and the final peak with the highest ozone values at 7.3 km may be accounted for in Figure 9d by one of the two folds of the tropopause present between 150 km and 300 km.

[40] One feature in the measurements not fully explained by either the mesoscale or global trajectories is a thin moist layer encountered by the aircraft just below G-D-E, with $\mathcal{H}$ = 50–100%, (the thick line in this area on Figure 9a). The mesoscale back trajectories show that air in this region has been following a level trajectory over the previous 24 hours (Figure 10a), although it is sandwiched between descending regions, which is not inconsistent with the high relative humidity encountered. This suggests that some interleaving of air masses of different origin is taking place on scales that are not resolved in this case by the global wind fields. The origin of air plot Figure 10a shows several separate maxima in the rates of descent in the dry intrusion and behind the front. These distinct maxima in descent rates are reminiscent of the mesoscale structures of the dry intrusion behind a surface cold front [*Browning and Golding*, 1995].

[41] Flight 6 was much less turbulent throughout compared to flight 1 (the scale for $\langle w'^2 \rangle$ in Figure 10b is 5× less than in Figure 5b), and turbulence encountered by the aircraft was largely confined to regions where the aircraft intersects the upper level front or is below 1 km. Perhaps surprisingly, lower turbulence leads to more mixing lines in the tracer scatterplots compared to flight 1. This is because anomalous layers persist, and undergo mixing on their upper and lower surfaces, for longer compared to flight 1. In the case of flight 1 such layers are more rapidly diluted by background tropospheric air until they are no longer detectable.

[42] Figures 11 and 12 show the tracer scatterplots for flight 6. In Figure 11, parcels are colored according to their measured θ_w, in order to contrast measurements taken ahead of and behind the front. Figure 11a shows the r_T:θ_w and contains the key to the symbols used. Figure 11b shows the O_3:CO scatterplot, and it shows substantial clustering of points according to θ_w. For instance, the airmass sampled on the highest leg of the flight (blue diamonds) has distinctly lower ozone than elsewhere. Air sampled at low levels in the planetary boundary layer (red crosses) has a negative O_3:CO correlation, including some comparatively high CO concentrations of up to 190 ppbv and low ozone (20 ppbv). This is characteristic of recently polluted air in which O_3 has been titrated in the presence of NO_x. In the winter, one would expect the negative O_3:CO correlation to persist as the air aged [*Parrish et al.*, 2000], but in April, greater photochemical activity may lead to subsequent ozone production in this airmass. Very high levels of NO_x were recorded on the two occasions the aircraft flew at low levels above the North Sea (up to 31 and 10 ppbv, respectively, on each occasion) suggesting that the pollution episodes were very recent. Of the free troposphere measurements, three separate negative O_3:CO correlations can be detected in (1) the air behind the front (orange stars), (2) dry intrusion air above and ahead of the front (cyan diamonds), and (3) upper level air (blue triangles) encountered during the uppermost leg of the flight. The remaining measurements made near the upper level front have no distinct pattern to the correlations. Figure 11c is the r:O_3 plot, and as in the case of flight 6, this plot forms an L-shaped pattern. Compared with flight 1, many points lie in the "mixing line" area of the diagram, between the vertical tropospheric branch and the horizontal stratospheric (or upper tropospheric) branch. We will argue below that this is due to the mixing of the lower layer of upper tropospheric signature air with background air at A/I/J and F.

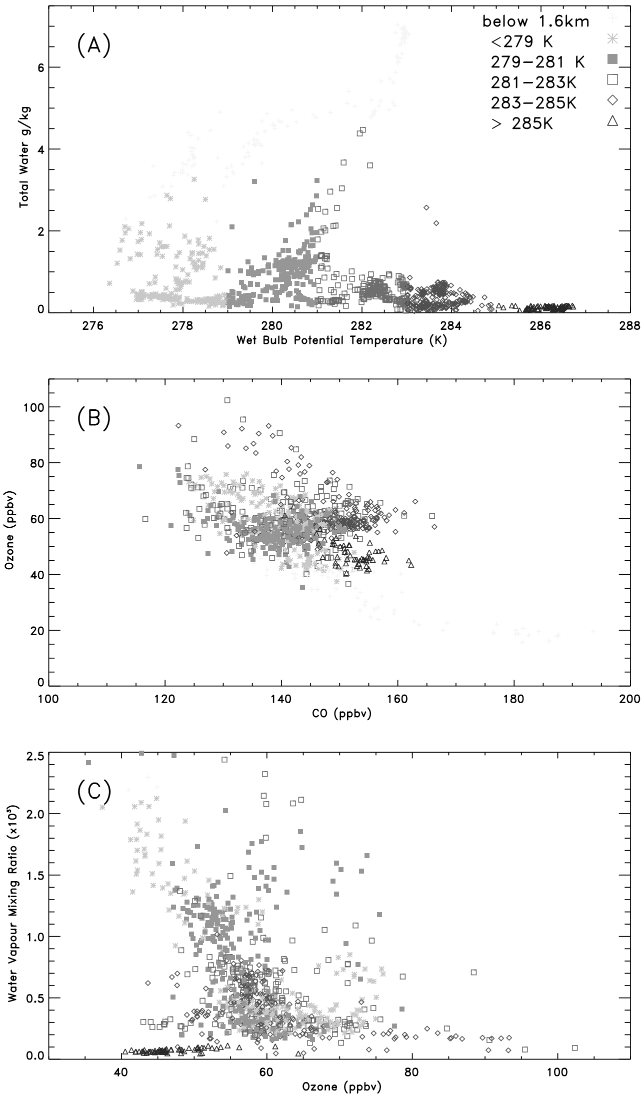

Figure 11. Tracer-tracer scatterplots for flight 6. Points are colored according to their wet-bulb potential temperature θ_w (see key) or they are colored red if below 1.6 km. (a) Total water r_T:θ_w. (b) O_3:CO. (c) Water vapor mixing ratio r:Ozone. See color version of this figure at back of this issue.

[43] Figure 12 shows higher temporal resolution (10 s) measurements in the features A–J. Figure 12a shows the O_3:CO scatterplot, revealing that both the G-D-C-E-B-H feature and the A/I/J feature have distinct, relatively compact, negative O_3:CO relationships, providing further evidence that we are sampling the same airmass several times in each case. The deviation from this characteristic O_3:CO ratio of some of the yellow points can be interpreted as mixing with background air at H. The global scale back trajectories indicate that the G-D-C-E-B-H feature, the A/I/J feature and F have origin near the tropopause. Negative O_3:CO correlations are consistent with an upper tropospheric-lower stratospheric origin, although polluted air in the winter may have a similar negative correlation due to ozone titration [*Parrish et al.*, 2000]. However, NO_y and CO (not shown) are negatively correlated in each feature, which indicates stratospheric influence rather than pollution. The high levels of CO in the G-D-C-E-B-H feature point toward an upper tropospheric rather than a stratospheric origin.

[44] Figure 12b shows the r:O_3 relationship, and following the arguments made for flight 1, it is clear that the A/I/J feature (red points) has undergone considerable mixing, particularly at A where the $r > 1.5\mathrm{g\ kg}^{-1}$ samples were taken. If the F feature (orange points) is indeed of upper tropospheric origin (as indicated by the global scale back trajectories), then it also appears to have undergone mixing. Consistent with this the aircraft encountered several turbulent patches near F (Figure 10b). By contrast the G-D-C-E-B-H filament appears relatively unmixed, except at H, and at the lower surfaces of E and G, where mixing with the thin moist layer discussed above appears to have taken place. (This explains the mixing line present in the dark blue points.) Unlike the flight 1 case, trajectory

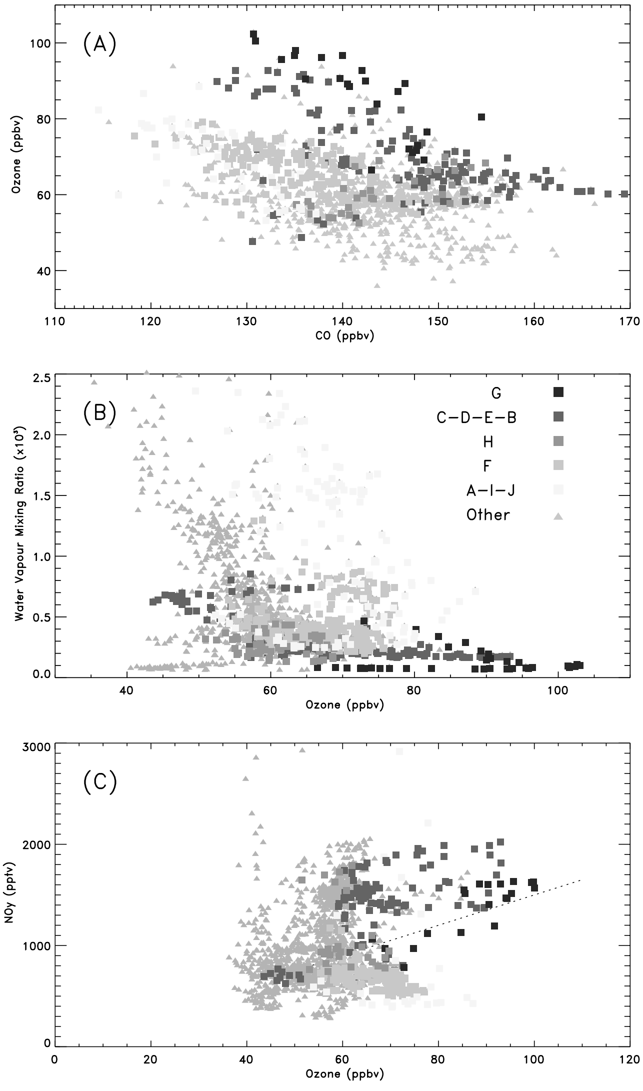

Figure 12. As in Figure 11 but with points colored according to the features of interest described in the text (see key). (a) O_3:CO. (b) r:O_3. (c) NO_y:O_3. See color version of this figure at back of this issue.

histories cannot be used to make lower bounds on dilution levels as the parcels have not recently seen sufficiently cold temperatures.

[45] Figure 12c shows NO_y:O_3 scatterplots for regions where the peaks in ozone were measured. Tropospheric NO_y:O_3 ratios are known to vary widely [*Murphy et al.*, 1993], but recently, *Fischer et al.* [2000] have produced some characteristic ratios for the lowermost stratosphere. These vary from 0.004 for the stratosphere proper to 0.015 for the lowermost stratosphere (dotted line in Figure 12c). It is notable that the G-D-C-E-B-H filament samples lie close to this dotted line, although this may not be taken as evidence of lower stratospheric origin owing to the relatively high CO levels present in the filament. Low values of NO_y:O_3 (e. g. red points from A–I–J) are likely to have been caused by mixing with marine boundary layer air, which has a low characteristic ratio.

5.2. Warm Conveyor Belt

[46] Figure 10a shows the Lagrangian rate of change of altitude of the air parcels in the frontal zone, according to the mesoscale back trajectories averaged over the previous 30 hours. The WCB is apparent in the mid-to-upper troposphere as a narrow ascending airstream, with a width of the order of only 50 km. Again, a similar pattern is obtained from the global trajectories, but with weaker ascent rates in the middle of the WCB jet, perhaps due to lower wind resolution.

[47] Unlike flight 1, flight 6 did not pass through the upper part of the WCB, so it is not possible to use the r_T:θ_w scatterplot to compare the stratification within the WCB with that observed during flight 1. It is notable, however, that many of the measurements in the region 1.6–3 km above the region of the surface front cluster around $\theta_w = 281$ K and $r_T = 1$ g kg^{-1}, indicating a well-mixed convecting region in which the aircraft has also encountered turbulence (see the regions ahead of and below A–I–J in Figure 10b).

[48] Comparing the extent of the WCB between case studies (250 km in the flight 1 case and 50 km for flight 6) and the corresponding ascent rates (up to 8 km day^{-1} for flight 1 compared with 3 km day^{-1} here), it is clear that there is large contrast in the upward mass flux between the two WCBs. These mass fluxes have been calculated directly from the mesoscale trajectories and are calculated to differ by a factor of 8, with the upward mass flux per unit distance along the front calculated to be 4×10^{12} kg day^{-1} km^{-1} (flight 1 case) case) and 5×10^{11} kg day^{-1} km^{-1} (flight 6 case).

[49] As noted by several authors [*Stohl*, 2001; *Cooper et al.*, 2001; *Kowol-Santen et al.*, 2001], the WCB is a potent mechanism for transporting anthropogenic pollution from the planetary boundary layer into the free troposphere. These case studies illustrate that variation in WCB transport between cyclonic systems may be strongly coupled with variation in the transport and mixing properties of the dry intrusion airstream.

6. Conclusions

[50] Labeling the two case studies “Intense Surface Low” (ISL) for Flight 1 on 16-01-99 and “Weak Surface Low” (WSL) for Flight 6 on 10-04-99 our conclusions are as follows:

1. In the surface front region the strong gradient in θ_w, which defines the surface front, was found in both the ISL and WSL cases to extend upwards for 2.5–3 km. Regions of strong turbulence, defined by large variances in the high-frequency measurements of the vertical wind, were encountered by the aircraft as it passes through this region, indicating convective mixing. Behind the surface front region, and above 3 km, an upper level front that increased in height moving away from the surface front with an aspect ratio of 150–250:1. Patches of turbulence were also encountered by the aircraft in the region of the upper level front, particularly in the ISL case, where w'^2 variances were typically 10× greater than in the WSL case. Saturated conditions and turbulence at the surface front and upper level front are consistent with line convection and slantwise convection, respectively, in these regions [see, e.g., *Browning*, 1990, Figure 8.8].
2. Trajectory analysis of each system revealed a deep airstream of rapidly ascending air directly above the surface front. These jet-like airstreams were identified as warm conveyor belts (WCBs), and measurements confirmed they contained saturated air low in ozone, consistent with a marine boundary layer origin. However, there was found to be a large contrast in the intensity of these jets with WCB vertical mass flux at 5 km greater in the ISL case by a factor of 8.
3. In the ISL system, where the aircraft passed through the WCB several times, much of the WCB was found to be stably stratified above the 4 km level. One sonde close to the surface front found neutral stratification up to 6 km, This suggests that although moderate turbulence was encountered in the upper WCB, transport is for the most part likely to be essentially slantwise. By contrast, the lower WCB is neutrally stratified and is likely to be ventilated by convection from the boundary layer.
4. In the region of the upper level front in both systems, trajectory analysis revealed the air to be either descending or moving on a relatively level trajectory. Within these regions were layers of trajectories that had previously had high PV (1–3 PVU), suggesting an origin in the lower stratosphere or upper troposphere near the tropopause. In the ISL system a single layer was identified, but a more complex layered structure was revealed by the global RDF trajectories in the WSL system. Measurements confirmed there was indeed a single dry, ozone-rich layer in the ISL system, but a complex layered structure in the WSL system, featuring at least three dry layers of enhanced ozone. Chemical measurements of CO and NO_y in the WSL case, however, indicated that by chemical criterion the air in these layers was upper tropospheric.
5. Tracer scatterplot analysis, backed up by considerations regarding the saturation mixing ratio history of each parcel, suggest that the ozone-rich layer in the ISL system was strongly mixed and diluted as it descended into the midtroposphere from the tropopause region. By contrast there was little evidence for mixing of the midtropospheric ozone-rich layer in the WSL system (at 5–6 km), although a lower ozone-rich layer (at 2.5 km) did appear to be undergoing mixing. This is consistent with the much weaker turbulence measurements compared with the ISL system.

The ISL system may therefore be less effective at transporting ozone to the lower troposphere than the much weaker WSL system, because the ozone-rich air was mixed into the upper and midtroposhere by strong three-dimensional turbulence. This is in contrast to the much stronger upward transport in the ISL system WCB discussed above.

6. As stated above, there is evidence for strong mixing in the ISL case in the upper troposphere in the region of the dry intrusion. In contrast, in the WSL case the dry intrusion transports ozone-rich air downwards in a number of thin layers, with mixing only clearly identifiable in the lowest layer. These results have implications for the budgets of O_3 and HO_x in the free troposphere, which can be perturbed when, for example, O_3-rich air of stratospheric origin mixes with H_2O-rich tropospheric air [*Esler et al.*, 2001]. Lifetimes and mix-down times for stratospheric filaments are not well quantified but, based on these results, vary significantly between different frontal systems. Equally, the rate of upward transport of boundary layer air also varies between the WCBs of the two systems, see also the climatology of *Stohl* [2001]. In systems where the WCBs contain polluted air, the rate of entrainment of background tropospheric air will be important for the O_3 budget [*Wild et al.*, 1996], as will the rate of mixing with boundary layer air within the WCB due to the line convection at the surface front (see section 4.2). In this case the level of NO_x in the conveyor belt will be important. How long polluted conveyor belts remain chemically active once in the upper troposphere is still an open question. Our measurements and those of *Parrish et al.* [2000] suggest that in the winter and early spring most airmasses, whether of polluted or stratospheric influence, tend to have negative O_3:CO correlations consistent with a low level of photochemical activity.

7. The global RDF trajectories performed better than the mesoscale trajectories at reconstructing observed tracer features (compare Figures 4c and 4d, 9c and 9d), despite the much higher resolution of the mesoscale winds. This seems to be due to the limited domain problem of the mesoscale trajectories. The mesoscale trajectories cannot detect differences in parcel origin for parcels whose back trajectories diverge outside the model domain.

[51] **Acknowledgments.** DCFZ was a project funded through the NERC UTLS Ozone Programme. Flight 6 was cofunded through the EU MAXOX project (ENV4-CT97-0525). During writing, J.G.E. was supported by NERC Fellowship NER/I/S/1999/00137. We are grateful to members of the MAXOX consortium for their help in the planning and execution of this flight and in particular aircraft scientists P.S. Monks and A. Kaye. The authors would also like to thank Peter Panagi and Ed Dicks for providing mesoscale forecasts and help with the mesoscale trajectory model. Discussions with Danny Chapman, Keith Browning, Mat Evans, Geraint Vaughan, Ed Pavelin, and Rob Mackenzie are gratefully acknowledged.

References

Bethan, S., G. Vaughan, C. Gerbig, A. Volz-Thomas, H. Richer, and D. A. Tiddeman, Chemical air mass differences near fronts, *J. Geophys. Res.*, *103*, 13,413–13,434, 1998.

Bithell, M., L. J. Gray, and B. D. Cox, A three-dimensional view of the evolution of midlatitude stratospheric intrusions, *J. Atmos. Sci.*, *56*, 673–687, 1999.

Bolton, D., The computation of equivalent potential temperature, *Mon. Weather Rev.*, *108*, 1046–1053, 1980.

Browning, K. E., Organisation of clouds and precipitation in extratropical cyclones, in *Extratropical Cyclones–The Erik Palmén Memorial Volume*, pp. 129–153, Am. Meteorol. Soc., Boston, Mass., 1990.

Browning, K. E., and B. W. Golding, Mesoscale aspects of a dry intrusion within a vigorous cyclone, *Q. J. R. Meteorol. Soc.*, *121*, 463–493, 1995.

Browning, K. E., N. M. Roberts, and A. J. Illingworth, Mesoscale analysis of the activation of a cold front during cyclogenesis, *Q. J. R. Meteorol. Soc.*, *123*, 2349–2375, 1997.

Brunner, D., J. Staehelin, and D. Jeker, Large-scale nitrogen oxide plumes in the tropopause region and implications for ozone, *Science*, *282*, 1305–1309, 1998.

Carlson, T. N., Airflow through midlatitude cyclones and the comma cloud pattern, *Mon. Weather Rev.*, *108*, 1498–1509, 1980.

Chaumerliac, N., R. Rosset, M. Renard, and E. C. Nickerson, The transport and redistribution of atmospheric gases in region of frontal rain, *J. Atmos. Chem.*, *14*, 43–51, 1992.

Cooper, O. R., J. L. Moody, J. C. Davenport, S. J. Oltmans, B. J. Johnson, X. Chen, P. B. Shepson, and J. T. Merrill, Influence of springtime weather systems on vertical ozone distribution over three North American sites, *J. Geophys. Res.*, *103*, 20,001–20,013, 1998.

Cooper, O. R., et al., Trace gas signatures of the airstreams within North Atlantic cyclones: Case studies from the NARE'97 aircraft intensive, *J. Geophys. Res.*, *106*, 5437–5456, 2001.

Donnell, E. A., D. J. Fish, E. M. Dicks, and A. J. Thorpe, Mechanisms for pollutant transport between the boundary layer and the free troposphere, *J. Geophys. Res.*, *106*, 7847–7856, 2001.

Emanuel, K. A., *Atmospheric Convection*, chap. 3, Oxford Univ. Press, New York, 1994.

Esler, J. G., D. G. H. Tan, P. H. Haynes, M. J. Evans, K. S. Law, P. H. Plantevin, and J. A. Pyle, Stratosphere–troposphere exchange: Chemical sensitivity to mixing, *J. Geophys. Res.*, *106*, 4717–4731, 2001.

Fischer, H., F. G. Weinhold, P. Hoor, O. Bujok, C. Schiller, P. Siegmund, M. Ambaum, H. A. Scheeren, and J. Lelieveld, Tracer correlations in the northern high latitude lowermost stratosphere: Influence of cross-tropopause mass exchange, *Geophys. Res. Lett.*, *27*, 97–100, 2000.

Gerbig, C., S. Schmitgen, D. Kley, A. Volz-Thomas, K. Dewey, and D. Haaks, An improved fast-response vacuum-UV resonance fluorescence CO instrument, *J. Geophys. Res.*, *104*, 1699–1704, 1999.

Gimson, N. R., Dispersion and removal of pollutants during the passage of an atmospheric frontal system, *Q. J. R. Meteorol. Soc.*, *120*, 139–160, 1994.

Grant, W. B., et al., A case study of transport of tropical marine boundary layer and lower tropospheric air masses to the northern midlatitude upper troposphere, *J. Geophys. Res.*, *105*, 3757–3769, 2000.

Hov, O., et al., Maximum oxidation rates in the free troposphere (MAXOX), Final Report, *Contract No. ENV4-CT97-0525*, Comm. of the Eur. Communities, Brussels, 2000.

Inverarity, G. W., Correcting airborne temperature data for lags introduced by instruments with two-time-constant responses, *J. Atmos. Oceanic Technol.*, *17*, 176–184, 1999a.

Inverarity, G. W., Flight Research Laboratory Kalman Filter/Rauch-Tung-Streibel smoother for inertial navigation correction and wind renavigation, I, Correcting horizontal position and velocity, *Meteorol. Res. Flight Internal Note 67*, U.K. Meteorol. Off., 1999b.

Kowol-Santen, J., M. Beekman, S. Schmitgen, and K. Dewey, Tracer analysis of transport from the boundary layer to the free troposphere, *Geophys. Res. Lett.*, *28*, 2907–2910, 2001.

Methven, J., Offline trajectories: Calculation and accuracy, *UGAMP Tech. Rep. 44*, Dep. of Meteorol., Univ. of Reading, England, 1997.

Methven, J., M. J. Evans, P. Simmonds, and T. G. Spain, Estimating relationships between airmass origin and chemical composition, *J. Geophys. Res.*, *106*, 5005–5019, 2001.

Murphy, D. M., D. W. Fahey, M. H. Proffitt, S. C. Liu, K. R. Chan, C. S. Eubank, S. R. Kawa, and K. K. Kelly, Reactive nitrogen and its correlation with ozone in the lower stratosphere and upper troposphere, *J. Geophys. Res.*, *98*, 8751–8774, 1993.

Newell, R. E., et al., Ubiquity of quasi-horizontal layers in the troposphere, *Nature*, *398*, 316–319, 1999.

Nicholls, S., J. Leighton, and R. Barker, A new fast response instrument for measuring total water, *J. Atmos. Oceanic Technol.*, *7*, 706–718, 1990.

Offiler, D., D. W. Johnson, W. D. N. Jackson, P. R. A. Brown, and A. L. Grant, Aircraft Winds Working Group Report, *Meteorol. Res. Flight Tech. Note 17*, U.K. Meteorol. Off., 1999.

Parrish, D. D., J. S. Holloway, R. Jakoubek, M. Trainer, T. B. Ryerson, G. Hübler, F. C. Fehsenfeld, J. L. Moody, and O. R. Cooper, Mixing of anthropogenic pollution with stratospheric ozone: A case study from the North Atlantic wintertime troposphere, *J. Geophys. Res.*, *105*, 24,363–24,374, 2000.

Peters, D., and D. W. Waugh, Influence of barotropic shear on the poleward advection of upper tropospheric air, *J. Atmos. Sci.*, *53*, 3013–3031, 1996.

Plumb, R. A., and M. K. W. Ko, Interrelationships between mixing ratios of long-lived stratospheric constituents, *J. Geophys. Res.*, *97*, 10,145–10,156, 1992.

Stohl, A., A one year Lagrangian “climatology” of airstreams in the northern hemisphere troposphere and lowermost stratosphere, *J. Geophys. Res.*, *106*, 7263–7280, 2001.

Stohl, A., and T. Trickl, A textbook example of long-range transport: Simultaneous observation of ozone maxima of stratospheric and North American origin in the free troposphere over Europe, *J. Geophys. Res.*, *104*, 30,445–30,462, 1999.

Stone, E., W. J. Randel, and J. L. Stanford, Transport of passive tracers in baroclinic wave life-cycles, *J. Atmos. Sci.*, *56*, 1364–1381, 1999.

Ström, J., and J. Heintzenberg, Water vapor, condensed water and crystal concentration in orographically influenced cirrus clouds, *J. Atmos. Sci.*, *51*, 2368–2383, 1994.

Sutton, R., H. Maclean, R. Swinbank, A. O’Neill, and F. W. Taylor, High resolution tracer fields estimated from satellite observations using Lagrangian trajectory calculations, *J. Atmos. Sci.*, *51*, 2995–3005, 1994.

Thouret, V., J. Cho, R. Newell, A. Marenco, and H. Smit, General characteristics of tropospheric trace constituent layers observed in the MOZAIC program, *J. Geophys. Res.*, *105*, 17,379–17,392, 2000.

Wang, K.-Y., and D. E. Shallcross, A Lagrangian study of the three-dimensional transport of boundary-layer tracers in an idealised baroclinic wave life-cycle, *J. Atmos. Chem.*, *35*, 227–247, 2000.

Weinstock, H., Energy dissipation rates of turbulence in the stable free atmosphere, *J. Atmos. Sci.*, *38*, 880–883, 1981.

Wernli, H., A Lagrangian-based analysis of extratropical cyclones, II, A detailed case study, *Q. J. R. Meteorol. Soc.*, *123*, 1677–1706, 1997.

Wernli, H., and H. C. Davies, A Lagrangian-based analysis of extratropical cyclones, I, The method and some applications, *Q. J. R. Meteorol. Soc.*, *123*, 467–489, 1997.

Wild, O., K. S. Law, D. S. McKenna, B. J. Bandy, S. A. Penkett, and J. A. Pyle, Photochemical trajectory modeling studies of the North Atlantic region during August 1993, *J. Geophys. Res.*, *101*, 29,269–29,288, 1996.

H. Barjat, K. Dewey, and J. Kent, Meteorological Research Flight, U.K. Met Office, DRA Farnborough, Hampshire GU14 6TD, England, U.K.

N. Brough, School of Environmental Sciences, University of East Anglia, Norwich, NR4 7TJ, England.

J. G. Esler, Department of Mathematics, University College London, Gower Street London, WC1E 6BT, England. (gavin@math.ucl.ac.uk)

P. H. Haynes, Department of Applied Mathematics and Theoretical Physics, Centre for Atmospheric Science, University of Cambridge, Silver Street, Cambridge, CB3 9EW, England. (P.H.Haynes@damtp.cam.ac.uk)

K. S. Law, Department of Chemistry, Centre for Atmospheric Science, University of Cambridge, Lensfield Road, Cambridge, CB2 1EW, England. (kathy.law@atm.ch.cam.ac.uk)

S. Schmitgen, Laboratoire des Sciences du Climat et de l’Environnement, UMR CEA/CNRS 1572, C.E. de l’Orme des Merisiers, 91191 Gif-sur-Yvette, Cedex, France.

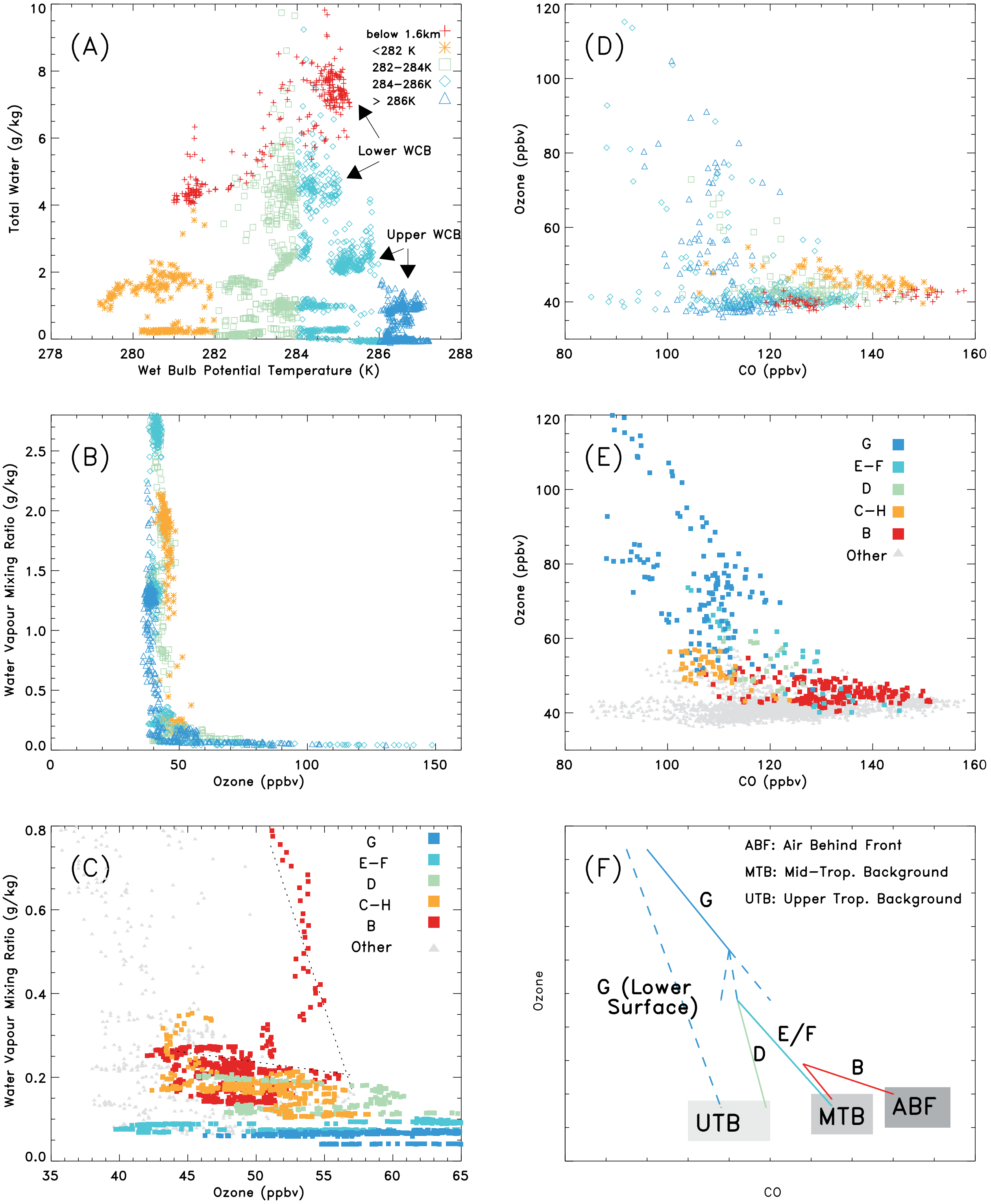

Figure 6. Tracer-tracer scatterplots of measurements made during flight 1. (a) Total water r_T:θ_w. (b) Water vapor mixing ratio r:Ozone, with parcels colored according to their measured θ_w. Parcels are plotted with temporal resolution 30 s. (c) As in Figure 6b but with parcels from the labeled features colored. A higher temporal resolution (10 s) is used. The dotted lines show mixing lines at measurement B. (d) O_3:CO with parcels colored according to their measured θ_w. (e) O_3:CO with parcels colored according to feature. (f) A schematic showing mixing effects in the O_3:CO plot; see text for details.

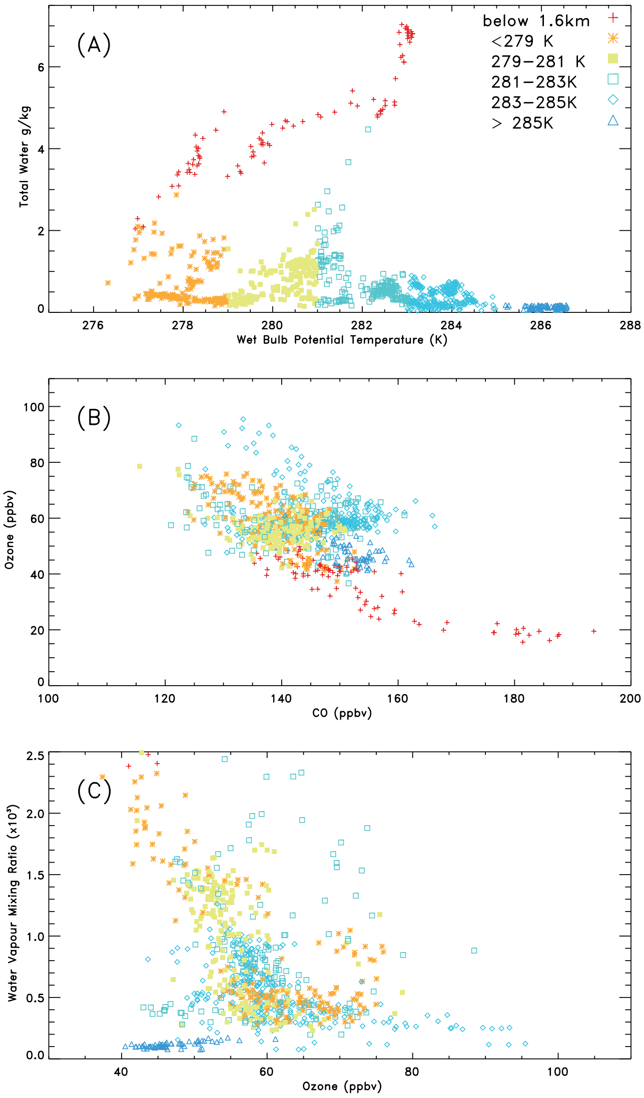

Figure 11. Tracer-tracer scatterplots for flight 6. Points are colored according to their wet-bulb potential temperature θ_w (see key) or they are colored red if below 1.6 km. (a) Total water r_T:θ_w. (b) O_3:CO. (c) Water vapor mixing ratio r:Ozone.

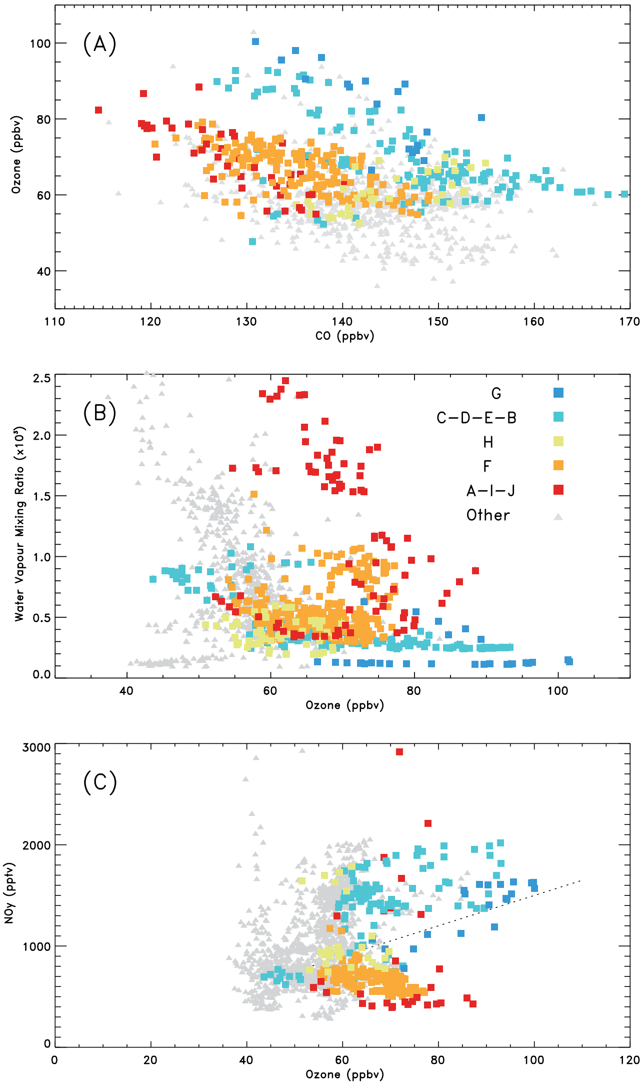

Figure 12. As in Figure 11 but with points colored according to the features of interest described in the text (see key). (a) O_3:CO. (b) r:O_3. (c) NO_y:O_3.